TORSIONAL DYNAMICS AND ROTATIONAL

ESTIMATION OF TIP-STEERABLE NEEDLES

by

John P. Swensen

A dissertation submitted to The Johns Hopkins University in conformity with the

requirements for the degree of Doctor of Philosophy.

Baltimore, Maryland

November, 2011

Abstract

In this dissertation, we present improvements to modeling of tip-steerable needles and new estimation techniques with applications to tip-steerable needles. Previous models of tip-steerable needles assumed the angles and velocities at the tip and base of the needle were equivalent. Such assumptions were simplifying, but not accurate. Additionally, to accurately control the trajectories of tip-steerable needles, the control algorithms must have accurate estimates of the position and orientation of the needle tip.

In the beginning of this dissertation, we derive the torsional dynamics of tip-steerable needles during continuous insertion. This is coupled with an existing kinematic model of tip motion to achieve a more faithful model. We describe the needle under torsion with a partial differential equation derived via the Newton force formulation. We use proper orthogonal decomposition to change coordinates to a different basis and Galerkin projection reduces this infinite dimensional system to a discrete number of ordinary differential equations in time only. We present several different practical modeling assumptions with associated controllers for attaining the objective

ABSTRACT

of control to a plane. We conclude by giving the results of physical experiments for one of the simplified models.

The latter portion of the dissertation develops new methods of observing the full attitude of the tip of the needle given the limited measurement of only the bearing of the needle tip. The contribution herein consists of an observer described as a matrix differential equation on the manifold SO(3) directly, rather than an observer for a coordinatization or embedding. Coordinatizations and embeddings necessarily introduce geometric and kinematic singularities, which this observer avoids. This new class of space-preserving observers are called invariant observers. We give an exact proof of almost global convergence of the estimator—the estimator will converge to the true orientation for all but a set of initial conditions of measure zero given a mild constraint of persistent excitation. We conclude by discussing the possibilities of extending the invariant observer to an optimal estimator, in the sense of Kalman filtering minimization of error covariance.

Primary Reader: Noah J. Cowan

Readers: Allison M. Okamura, Louis L. Whitcomb

Acknowledgments

There are two people whose influence most helped me reach this point: my wife Brittney and my advisor Professor Noah Cowan.

If I were a degree conferring institution, Brittney would be simultaneously receiving a doctoral degree in *something* for all she has done over the last five years; many stretches of which she was a graduate school widow. I will forever be grateful for her willingness to give up a home, a good job, and comfortable life to return to school to pursue my dreams. Without her patience, encouragement, hard work, and love I could not have achieved this.

Noah's passion for learning is contagious, his incessant desire to tackle hard problems is inspirational, and his ability to help me guide my research according to my unique skill set was exact. During my early years he guided me to work that allowed me to use my pre-existing skills from industry while pushing me to learn those things I struggle with; his approach was perfectly tailored to my abilities. His ability to ascertain exactly *how* I was having trouble understanding and his patience when it took me longer than it should have to "get it" helped me to grow into a more complete

ACKNOWLEDGMENTS

Dedication

This thesis is dedicated to my parents, Richard Hunter Swensen and Helen Thompson Swensen. They instilled in all of their children a love of learning and the value of hard work.

Contents

CONTENTS

CONTENTS

CONTENTS

List of Tables

List of Figures

Chapter 1

Introduction

1.1 History of Needle Interventions

Percutaneous interventions play a critical role in modern medicine. Despite the ubiquity of needle-based procedures, clinical needle interventions are largely based on Alexander Wood's nineteenth century idea: delivery therapy subcutaneously through the lumen of sharp, stiff tubes [52]. There have been many new and exciting integrated systems for deploying needles, but remarkably little advancement in the needle insertion mechanism itself until recently. Notwithstanding these research advances, clinical interventions continue to rely primarily on straight insertion of steel needles. Recent exploration into steerable needles shows promise to improve existing procedures and help devise new procedures as needle steering improves [12, 42].

On the contrary, the flexible catheter which was invented at approximately the

same point in history, has evolved significantly since its crude beginnings. Figure 1.1 provides a side–by–side history of needles and catheters. Obviously, needles and catheters are used for distinctive purposes even though both are considered minimally invasive therapies. Needles are used for penetrating tissues via the cutting at the tip while catheters traverse existing channels in the body. As evidenced by the many procedures that can be accomplished through straight needle insertions, traditional rigid steel needles have served their purpose adequately for the past 250 years. However, new medical imaging technologies, advancements in control system theory, and the vast computational power at the disposal of researchers and clinicians open the doors to a vast, new array of potential interventions. Herein, we present new models to improve the control of our approach to tip-steerable needles.

Herein, we present advancements to the modeling of tip-steerable needles. The improvements are related to taking the existing kinematic model and adding the torsional dynamics associated with twisting these long, slender, super-elastic nitinol needles. Because steerable needles are neither rigid needles nor catheters, the primary objectives of needle steering research should be to first find methods of improving controllability and repeatability (here controllability does not refer to the well-defined notion of control systems, but instead a overarching description of the ability to get a steerable need to achieve high level task specification). The next logical step, which in some cases can be done simultaneously, is to work with clinicians to identify new procedures (or modifications of existing procedures) for which steerable needles provide
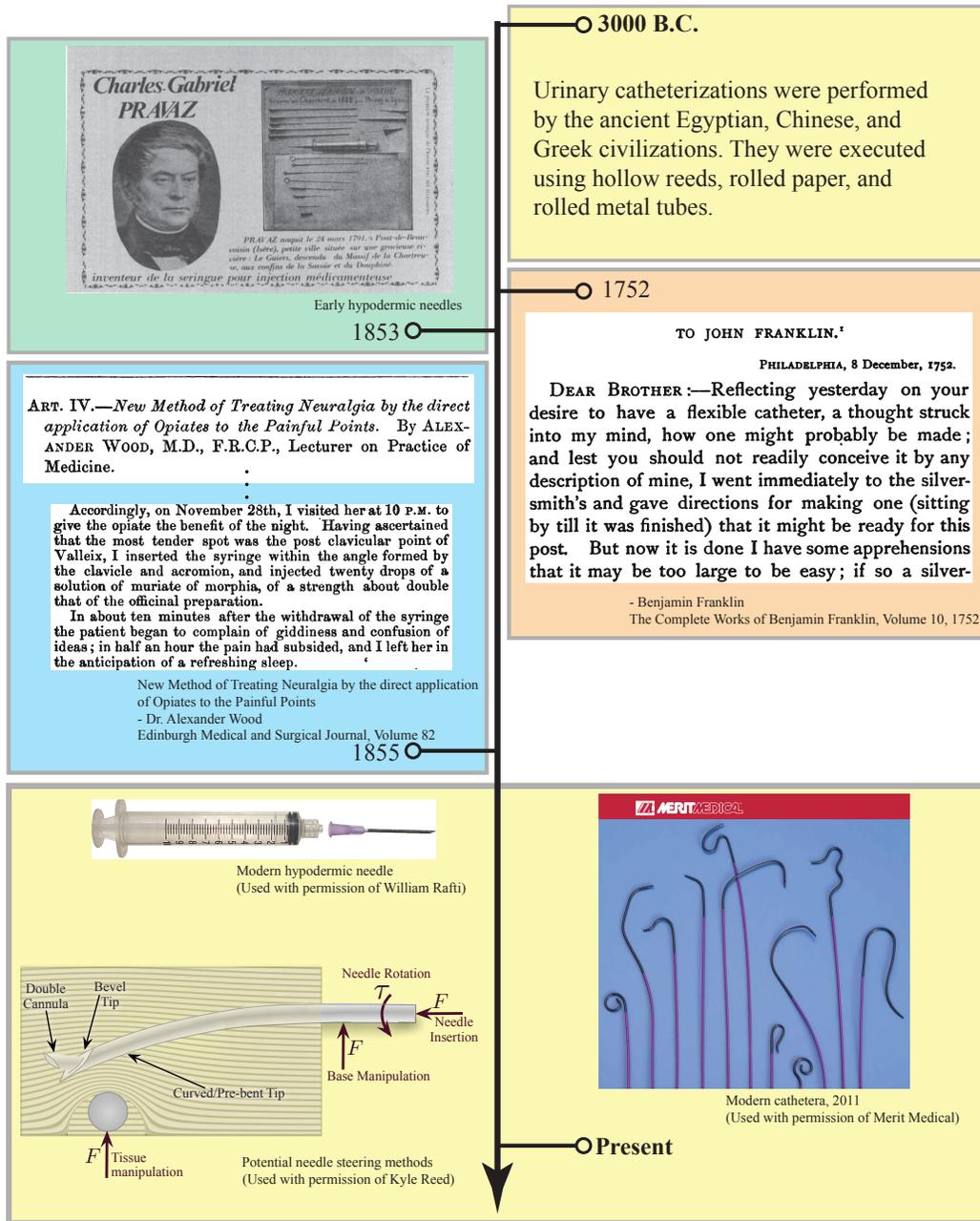
Figure 1.1: A timeline of the progress in hypodermic needles and catheters over time. Despite the advent of many new needle procedures, needle therapies still largely consist of delivery through straight steel tubes. On the other hand, new catheters are designed when new procedures are devised. The promise of needle steering is to move percutaneous therapies via needles into a "post-Wood" era of needle interventions.

a clear advantage. We believe that the work we present here helps prove that the field of steerable needles is somewhere past the point of proof of concept and viability and nearing the point where needle design, insertion mechanism, and clinical application need to be the motivating factor in order to advance the science. In particular, the work presented in this dissertation help push forward the controllability and repeatability of the tabletop experiments and solidify the belief that steerable needles can provide advantages over existing straight needle technologies. The fundamental contributions of this portion of the dissertation are (1) three different models of torsional dynamics for tip-steerable needles and (2) a proposed control law for controlling the needle tip to a virtual plane.

1.2   History of Invariant Attitude Estimation

As needle interventions move toward this new paradigm with associated automatic control, supervised-automatic control, or teleoperation, it is critical that the control methods have accurate estimates of the state of the needle. Many developments in control theory over the past 50 years have been driven by the desire for better attitude determination and control. Much of this work focuses on satellite attitude regulation, but estimation and control on the rotation group applies to a wide range of problems. Our particular treatment of the attitude estimation problem is motivated by a proposed technique for medical interventions to control tip-steerable needles [42, 50]. The heart of our problem lies in estimating all three degrees of freedom

of rotation given only a two degree-of-freedom measurement in the form of a unit vector—in our case, this unit vector corresponds to one of the columns of the rotation matrix. The goal is to determine the entire rotation matrix asymptotically, given that measurement plus knowledge of the control input.

This application drives the need for an estimator on SO(3) from measurement restricted to S^2, a result that could apply to any number of other fields involving attitude estimation for rotating rigid bodies. For example, attitude estimation in an underwater vehicle based on a gravity sensor or compass heading comes to mind. We demonstrate an essentially global estimator for this problem; convergence only fails for initial estimates that are π radians away from the actual state—a set of measure zero. The proof of convergence is given using (local) exponential coordinates that are valid over the entire domain of attraction. The method extends easily to the measurement of multiple vectors, for which the convergence proof becomes trivial. Our estimator is invariant in the sense that it is described by a matrix differential equation with the property that when the initial condition is on the manifold described by the Lie group SO(3), exactly integrating the matrix differential equation will result in the estimate remaining in SO(3) for all time. The fundamental contribution of this portion of the dissertation is an exact deterministic observer for the attitude of a rotating rigid body that (1) does not suffer from problems associated with observers for coordinatized systems and (2) is almost globally convergent even with limited measurements.

The vast majority of the past five decades since the advent of the Kalman filter, even nonlinear system that are relatively well understood (such as rigid body motion) have been wrangled into a form amenable to applications of the Kalman filter, through coordinatization and linearization. As the real world is inherently nonlinear, this technique has been the workhorse of the estimation and control systems for spacecraft, aircraft, submarines, and essentially every other noisy nonlinear system, and has performed admirably. However, despite working well, the method is fraught with pitfalls of divergence and singularities in representation and statistics [14, 30]. An exhaustive survey of the history of attitude filtering methods, with particular interest in nonlinear methods, is presented by Crassidis et al. [13].

Early work in nonlinear filters by Benes 1981 and Fred Daum 1986 tried to find generalizations of the Kalman filter as "exact" filters for certain classes of nonlinear systems. Their definition of exactness of a filter is whether they require solutions to ordinary differential equations instead of solutions to the partial differential equations. In fact, in Daum's excellent tutorial paper entitled "Nonlinear Filters: Beyond the Kalman Filter" [15] he states: "This is at the heart of the nonlinear filtering problem, because if we can solve the Fokker-Planck Equations (FPE) exactly in terms of Ordinary Differential Equations (ODE), then engineers can implement the nonlinear filter in real time." That is, if we can define invariant filters akin to the recent developments in invariant estimators, and solve the corresponding Fokker-Planck equations analytically, we will have achieved an almost global, optimal, invariant filter that

doesn't suffer from the curse of dimensionality. In some sense, this is the holy grail of nonlinear filtering for systems evolving on finite dimensional matrix Lie groups. We feel it has been the efficacy of the Kalman filter, and the apparent difficulty in solving Fokker-Planck equations on Lie groups, that has delayed the development of the invariant estimator.

In the search for an optimal invariant estimator with robustness to initial error, it appears the field is taking the opposite route to Kalman and Luemberger, where the stochastic and deterministic cases were treated in that order in 1961 and 1964, respectively. Cite the work by Salcudean. Recent work by Bonnabel et al. [6] and Mahoney et al. [31] have begun to develop a principled framework for defining invariant observers, with the requisite theorems that generalize the technique of finding convergent estimators. Markley [34] attempted to extend invariant observer to the status of a filter, but the tools to solve the FPE were not available and many simplifying assumptions were made. The natural next step is to develop invariant filters evolving from these invariant observers, as Kalman filters are to Luenberger observers. Recent work in stochastic processes on matrix Lie groups by Park and Chirikjian [10,40] may provide the tools necessary to solve the FPE, where it was previously not possible.

Chapter 2

Mathematical Background

Differential geometry is a natural way of describing continuous systems. Whether it be continuity in space and time (e.g. for describing the motion in time of a rigid bodies) or continuity in space and parameters (e.g. for describing the distribution of mass and inertia tensor for rigid bodies), differential geometry and differentiable manifolds provide a concise and standard form of describing, manipulating, and performing computations for continuous system. A particularly eloquent argument for the use of differential geometry as the language of continuous systems was given by Epstein:

> If Mathematics is the language of Physics, then the case for the use of Differential Geometry in Mechanics needs hardly any advocacy. The very arena of mechanical phenomena is the space-time continuum, and a continuum is another word for a differentiable manifold. Roughly speaking, this foundational notion of Differential Geometry entails an entity that can support smooth fields, the physical nature of which is a matter of context. In Continuum Mechanics, as opposed to Classical Particle Mechanics, there is another continuum at play, namely, the material body.

> This continuous collection of particles, known also as the body manifold, supports fields such as temperature, velocity and stress, which interact with each other according to the physical laws governing the various phenomena of interest. Thus, we can appreciate how Differential Geometry provides us with the proper mathematical framework to describe the two fundamental entities of our discourse: the space-time manifold and the body manifold. [18, Chapter 1: The Case for Differential Geometry]

In this section, we provide a mathematical background of the differential geometry for describing the manifolds associated with rigid body motion as matrix Lie groups and their associated Lie algebras. We also give the relationship between these geometrical concepts of manifolds and the coordinates chosen to represent manifolds locally. Similarly, with coordinates already chosen for the representation of the torsional states of a rotating rod, we present methods of changing coordinates and truncating coordinates to arrive at finite dimensional approximate representations of the torsional dynamics. This presentation is neither exhaustive nor rigorous in terms of content or proofs; it provides just enough background for understanding the notation and content of the remainder of this dissertation. We refer the reader to classic texts on differential geometry [1, 46], robotics in the language of differential geometry [11, 36], and continuum mechanics [22, 35] for a more thorough treatment of the subjects.

2.1 The Differential Geometry of Rigid Bodies

In robotics, the special orthogonal and special Euclidian groups are often used to describe the rotation and rotation plus translation of rigid bodies—using SO(3) and

$$\mathfrak{so}(3) \overset{\exp}{\underset{\log}{\rightleftarrows}} SO(3) \qquad \text{Rotations}$$

$$\mathfrak{se}(3) \overset{\exp}{\underset{\log}{\rightleftarrows}} SE(3) \qquad \text{Rotations and translations}$$
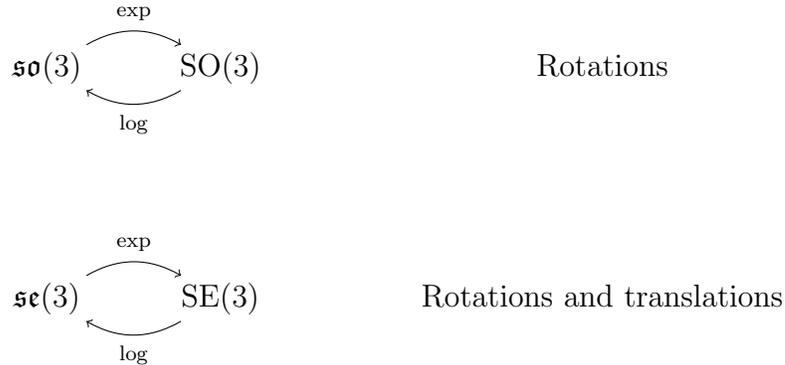
Figure 2.1: The relationship between the Lie groups and Lie algebras for rigid body motion.

SE(3) respectively. Each of these groups is also a matrix Lie group with its associated Lie algebra, $\mathfrak{so}(3)$ and $\mathfrak{se}(3)$ respectively, and corresponding bracket operator. These groups are classified as Lie groups because elements of the group are generated by the elements of the associated Lie algebra via the matrix exponential as seen in Figure 2.1. See Appendix A for definitions of groups, Lie algebras, and bracket operators.

For a general finite dimensional matrix Lie group, the tangent space of the Lie group can also be related to the Lie algebra via a left translation or right translation by a group element. Let $h \in G$ be a element of the lie group G with tangent space denoted $T_h G$ and tangent bundle TG. Given a Lie group G with Lie algebra $\mathfrak{g}$ and $f(h) \in T_h G$ a vector field on G, the tangent space at the identity configuration can be written as

$$h^{-1} f(h) = \hat{\xi} \in \mathfrak{g}$$

or

$$f(h)h^{-1} = \hat{\Xi} \in \mathfrak{g},$$

for the left and right translation respectively. Here, $\hat{\xi}$ or $\hat{\Xi}$ are the left- and right-invariant representations of the vector field $f(h)$ represented in the tangent space of the Lie group at the identity configuration, T_eG. Through the left/right translation, $\hat{\xi}$ and $\hat{\Xi}$ are both elements of the Lie algebra associated with the Lie group. This left/right translation is most often used in robotics to write the body-fixed frame velocities or spatial frame velocities of a moving rigid body. Associated with the Lie algebra (and tangent space at the identity) is an isomorphism between the algebra and the real Euclidean space

$$\hat{} : \mathbb{R}^n \to \mathfrak{g}$$

$$\vee : \mathfrak{g} \to \mathbb{R}^n,$$

(2.1)

for an n-dimensional Lie group and algebra. For all finite-dimensional matrix Lie groups, the bracketing operation for two elements of the Lie algebra is written as

$$\forall \hat{x}, \hat{y} \in \mathfrak{g}, \text{ then } [\hat{x}, \hat{y}] = \hat{x}\hat{y} - \hat{y}\hat{x}.$$

Specifically in this dissertation, we restrict ourselves to consider the groups SO(3) and SE(3). The group of rigid body rotation is defined as

$$\text{SO}(3) = \left\{ R : R \in \mathbb{R}^{3\times3}, R^T R = I, \det(R) = 1 \right\}$$

a three-dimensional manifold. Its Lie algebra is denoted as

$$\mathfrak{so}(3) = \left\{ \hat{\omega} : \hat{\omega} \in \mathbb{R}^{3\times3}, \hat{\omega} = -\hat{\omega}^T \right\}.$$

The group of all rigid body motions is defined as

$$\mathrm{SE}(3) = \left\{ \bar{g} = (p, R) : p \in \mathbb{R}^3, R \in \mathrm{SO}(3) \right\},$$

a six-dimensional manifold. Herein, we equate elements of SE(3) with their homogeneous matrix representation

$$g = \begin{bmatrix} R & \mathbf{p} \\ \mathbf{0}^T & 1 \end{bmatrix}.$$

Its Lie algebra is denoted as

$$\mathfrak{se}(3) = \left\{ \hat{\xi} = \begin{bmatrix} \hat{\omega} & \mathbf{v} \\ \mathbf{0}^T & 0 \end{bmatrix} : \hat{\omega} \in \mathfrak{so}(3), \mathbf{v} \in \mathbb{R}^3 \right\}.$$

The rigid body velocities represented in the body-fixed frame and spatial frame for rigid body rotation and rigid body rotation with translation are

$$\mathrm{SO}(3) \begin{cases} \text{(body-fixed frame velocities)} & R^T \dot{R} = \hat{\Omega} \\ \\ \text{(spatial frame velocities)} & \dot{R} R^T = \hat{\omega} \end{cases}$$

and

$$\text{SE(3)} \begin{cases} \text{(body-fixed frame velocities)} & g^{-1}\dot{g} = \hat{V} \\ \\ \text{(spatial frame velocities)} & \dot{g}g^{-1} = \hat{v}. \end{cases}$$

A common practice in robotics for working with rigid bodies is to frame the mathematics in terms of local coordinates for SO(3) and SE(3). This is often done without regard for the underlying manifolds with the understanding that the bounds for which the local coordinates are valid must not be violated. While this is a common practice, we suggest that treating rigid bodies first as the abstract manifold and second with local coordinates for a neighborhood of points on the manifold provides a better understanding of the physical world. This approach avoids the introduction of geometric and kinematic singularities until the point at which a concrete computation is necessary (see the proof of convergence for the invariant estimator in Section 4.4.1) or the coordinates provide an intuitive manner to understand robot motion (see the coordinatization and state reduction for control to a plane in tissue in Section 3.2.3). In this dissertation, we use a mixture of the group and coordinate representations to describe the motion of steerable needles. However, wherever possible, we start with the topological space describing rigid body motion and use coordinate charts for these topological spaces considered as manifolds when necessary for computations. In all cases herein, when velocities are represented without resorting to coordinates they are given with respect to the body-fixed frame. When velocities are given with respect to coordinates, they are related to the body-fixed frame velocities through

the appropriate Jacobian. The Jacobian between the body-fixed or spatial frame and coordinate velocities depends wholly on the choice of coordinate chart for the manifold. See Appendix A.2 for an illustrative computation of the Jacobian relating X-Y-Z Euler angle velocities and body-fixed frame velocities. A similar procedure can be used for any choice of coordinates. For an extensive listing of coordinate choice and the associated Jacobians for rigid body rotations, see Chirikjian and Kyatkin [9]. For the methods of deriving Jacobians for joint variables for open kinematic chains, see Murray et. al. [36].

2.2 Proper Orthogonal Decomposition and Galerkin Projection

Partial differential equations (PDEs) are used throughout the chapter on torsional dynamics to describe the Newton force formulation of needle forces for the needle, continuous in both space and time. Finding closed-form solutions to PDEs is a very hard problem. There are certain classes of PDEs for which closed-form solutions already exist and it is an active area of research to extend this class of problems. Even when closed-form solutions exist, they are often have infinite dimensional representation and are not amenable to concrete computation. Alternatively, finite element methods are numerical techniques in which the problem space is approximated by finite elements for which the dynamics and boundary conditions are defined for each element. The

choice of finite element geometry and the corresponding boundary conditions have a significant effect on the stability and exactness of the solution. Similarly, there exist modal methods which provide a means of changing the coordinates of the original problem to coordinates more amenable to exact or approximate solutions. Usually associated with the modal methods is a model order truncation of the infinite dimensional representation of the system. Two very common partial differential equations in engineering are the Navier-Stoke equation for the flow of incompressible fluids,

$$\frac{\nabla P}{\rho} + \nu \nabla^2 \mathbf{u}, \tag{2.2}$$

where ν is viscosity, $\mathbf{u}$ is fluid velocity, P is pressure, and ρ is fluid density, and the Euler-Bernoulli beam equation for beam deflection,

$$\frac{\partial^2}{\partial x^2} \left(EI \frac{\partial^2 y}{\partial x^2} \right) = -\mu \frac{\partial^2 y}{\partial t^2} + F(x) \tag{2.3}$$

where E is Young's modulus, I is the area moment of inertia, y is the deflection of the beam at a point x, mu is related to the density, and $F(x)$ is the force applied at each point x along the needle. The partial differential equation used in this dissertation has the form of a third common PDE called the telegrapher's equation for a lossy

transmission line[1],

$$\frac{\partial^2 V}{\partial t^2} + (\alpha + \beta)\frac{\partial V}{\partial t} - c^2\frac{\partial^2 V}{\partial x^2} = -\alpha\beta u, \tag{2.4}$$

where α, β, and c are inductance and conductance parameters of the circuit describing the transmission line.

In this dissertation, we use the common practice in solving PDEs of finding the infinite dimensional representation of the PDE using an assumed modal solution and projecting back onto the first n-modes [8, 49]. The technique taken here is one technique among a broader field of proper orthogonal decomposition and subsequent Galerkin projection [22, 45]. When the assumed solution is separable in space and time, where the mode shapes are function of the spatial variable and the mode coefficients are functions of time

$$\theta(x,t) = \frac{1}{2}q_0(t) + \sum_{k=1}^{\infty} \psi_k(x)q_k(t) + \sum_{k=1}^{\infty} \phi_k(x)p_k(t), \tag{2.5}$$

the result of an n-th order Galerkin projection is a system of n ordinary differential equations (ODE) in time. This method of model order reduction is particularly apropos when the system has dissipative terms causing exponential decay for states with high wavenumber, which the torsional dynamics of our system satisfies. When the system does not separate in space and time, we find a decomposition where the mode shapes are function of the spatial variable and time with the mode coefficient

---

[1]Special thanks to Dr. Greg Chirikjian for identifying the form of our PDE as the telegrapher's equation.

functions of time only

$$\theta(x,t) = \frac{1}{2}q_0(t) + \sum_{k=1}^{\infty} \psi_k(x,t)q_k(t) + \sum_{k=1}^{\infty} \phi_k(x,t)p_k(t),\qquad(2.6)$$

and perform the Galerkin projection and verify that each projection results in an ODE in time only. Later we discuss the specific choices of mode shapes and coefficients for the problem of torsional dynamics of needles.

Inherently, finding an infinite sum that either exactly describes or approximates a continuous function in two variables, e.g. $\theta(x,t)$, is simply a change of coordinates to a set of coordinates that are more amenable to finding an exact solution. In the case where sinusoidal functions are used as the mode shapes, there are additional properties of the continuous function that must be satisfied—periodicity, sufficient smoothness, etc. A more detailed treatment of functional Fourier series decomposition can be found in a signals and systems text, e.g. [29]. Consider a generic partial differential equation in two variables, x and t, of the form

$$\sum_{i=0}^{m} \sum_{j=0}^{n} \alpha_{i,j} \frac{\partial^{i+j}\theta(x,t)}{\partial x^i \partial t^j} = F(x,t),\qquad(2.7)$$

where $\alpha_{j,k}$ is a weighting coefficient of the particular combination of partial derivatives and $F(x,t)$ is an applied force. We substitute the generic assumed solution from (2.6)

into the generic partial differential equation from (2.7), resulting in

$$\sum_{i=0}^{m}\sum_{j=0}^{n}\alpha_{i,j}\underbrace{\frac{\partial^{i+j}\left\{\frac{1}{2}q_0(t)+\sum_{k=1}^{\infty}\psi_k(x,t)q_k(t)+\sum_{k=1}^{\infty}\phi_k(x,t)p_k(t)\right\}}{\partial x^i\partial t^j}}_{\varphi_{i,j}}=F(x,t)\quad (2.8)$$

The process of Galerkin projection then consist of projecting the partial differential equation back onto the mode shapes. In the cases where the mode shapes are periodic, the projection need only be done over a single period. The projection back onto the mode shapes, $\psi_k(x,t)$ and $\phi_k(x,t)$, written in the modal coordinate representation given in (2.8), is

$$\int_{-\ell}^{\ell}\psi_k(x,t)\left(\sum_{i=0}^{m}\sum_{j=0}^{n}\alpha_{i,j}\varphi_{i,j}\right)dx=\int_{-\ell}^{\ell}\psi_k(x,t)F(x,t)dx$$
$$\int_{-\ell}^{\ell}\phi_k(x,t)\left(\sum_{i=0}^{m}\sum_{j=0}^{n}\alpha_{i,j}\varphi_{i,j}\right)dx=\int_{-\ell}^{\ell}\phi_k(x,t)F(x,t)dx,\quad (2.9)$$

where ℓ is the half period. When the mode shapes are a function of the spatial component only, projection onto each mode shape will integrate out the spatial component of the system dynamics and result in a system of ordinary differential equations that are functions of the mode coefficient and dependent on time only. There are specific cases when the mode shapes are a function of both the spatial variable and time variable for which Galerkin projection still results in a system of ordinary differential equation in time only. Unfortunately, the only way to determine if this desirable result will occur for a system of this type is to attempt the Galerkin projection. Fortunately

for the time-varying mode shapes we use subsequently for the torsional dynamics of

tip-steerable needles, the Galerkin projection achieves this desirable result.

Chapter 3

Torsional Dynamics of

Tip-steerable Needles

3.1 Introduction

In this chapter, we derive and demonstrate a new model for torsional dynamics which we couple with an existing kinematic model of tip-steerable needles described by Webster et al. [50] and Park et al. [39]. The primary purpose of the additional modeling of torsion is to improve the estimation and control of the needle tip; here we perform control to a plane during continuous insertion for comparison to previous work [25]. Most previous modeling and control of tip-steerable needles makes the assumption that the insertion and rotational velocities at the tip of the needle are equivalent to those at the base of the needle. However, to achieve the desired bending

of tip-steerable needles inside tissue, our needles are made of the super-elastic alloy nickel-titanium (nitinol). These super-elastic needles severely violates the assumption that base and tip velocities are equal, as shown in Reed et al. [43]. Intuitively, twisting a long slender beam from the controlled proximal end will result in torsional windup along the length of the needle. This realization motivates our development in this chapter of a system model that incorporates the torsional dynamics, so that an automatic feedback controller can be designed to compensate accordingly.

3.1.1 Related work

The foundational papers of DiMaio et al. [16], Okazawa et al. [37], and Webster et al. [50] identified the potential that steerable needles might have to changed the landscape of percutaneous therapies into a "post Wood era". DiMaio and Salcudean [16] were the first to investigate the effects of tissue deformation, needle cutting, and external manipulation to robotically controlled needles in artificial tissues. Okazawa et al. [37] provided the first known mechanism design for affecting needle motion inside tissue by engineering the needle itself; their design consisted of an outer straight tube and inner stylet with a preset fixed radius of curvature uses to cause bending during needle insertion. Webster et al. [50] modeled needles with beveled tips as a nonholonomic kinematic systems and validated this model in simulated tissues. Further work shows that this nonholonomic model remains valid for other types of needle designs where the primary objective is an asymmetric force at the tip of the

needle, in this case a pre-curved section at the tip of the needle [51].

While the approach given in this chapter extends the nonholonomic kinematic model developed by Webster et al. , there are other techniques employed to steer needles, such as transverse and "tip/tilt" motion outside the tissue [19], or manipulation of the tissue itself [33]. Combinations of these steering methodologies might ultimately be used in a single, integrated setup, as proposed in [42] (see Figure 2 therein). In any such system, torsional dynamics – like those considered in this chapter – will play a critical role in needle motion.

Kallem and Cowan [25] performed closed-loop control to a virtual plane inside the tissue via feedback linearization, assuming no torsional dynamics. Reed et al. [43] developed a model of torsional dynamics for a fixed length of needle inside the tissue and performed open-loop torsional compensation during large needle tip reorientations. Kallem and Cowan noted that the controlled behavior of the needles differed from the theoretical predictions in a way that suggested torsional dynamics may have been playing a role. Reed et al.'s work later confirmed the significance of needle torsion on needle dynamics. The work presented in this chapter builds on these two papers, incorporating both feedback control and a new model of torsional dynamics that incorporate both continuous insertion and length-varying torsional dynamics inside and outside the tissue.

Other work incorporates needle and needle-tissue dynamics, but these have typically focused on tissue deformation and have approached the modeling problem using

finite element methods [16] or simplified "virtual spring" models [19]. Here, we neglect tissue deformation, and focus our modeling effort on needle torsional wind-up, including the viscous drag between needle and tissue. Our approach uses a proper orthogonal decomposition, coupled with a Galerkin projection [22, 47], allowing us to side-step finite element techniques altogether. This approach gives us an alternative infinite dimensional representation of the hypothesized system dynamics, which can then be systematically reduced to a manageable form by truncating higher-order terms in the infinite-dimensional expansion. The higher order terms are reduced via the Galerkin projection and the error between the truncated system and the infinite dimensional system can be made arbitrarily small through the choice of truncation order. Our work is somewhat analogous to a time-varying modal approach used for approximating the dynamics of a spacecraft antenna as it is extended [49].

3.2 Modeling

3.2.1 Previous Models of Tip-Steerable Needles

Given the body-fixed frame at the tip of the needle, as shown in Figure 3.1, the kinematic model developed by Webster et al. [50] describes the motion of the needle using the bicycle model with a fixed turning radius. The insertion velocity at the base of the needle prescribes the forward velocity of the bicycle, and the rotational velocity at the base changes the orientation of the plane in which the bicycle travels.
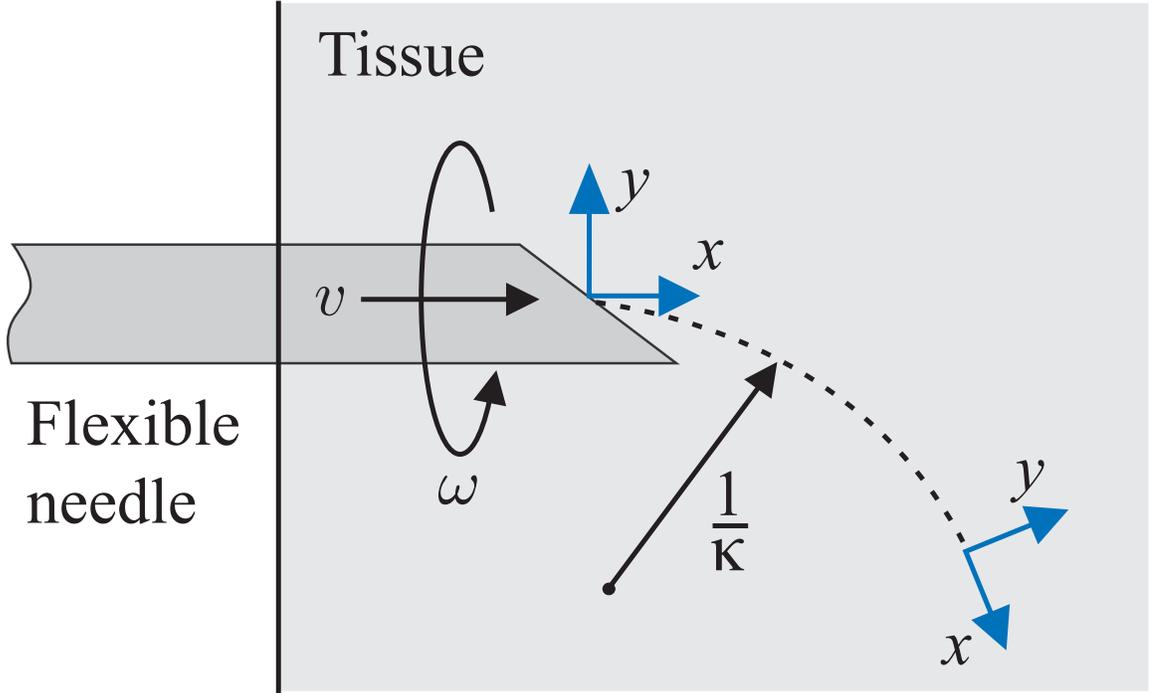
Figure 3.1: The kinematic model used to represent the insertion of tip-steerable flexible needles, adapted from [50]. As the needle is inserted at velocity v, a bevel or other tip asymmetry causes a lateral force that deflects the needle along a curved path of radius $1/\kappa$. Rotations about the tip with angular velocity ω reorient the bevel tip (Modified with permission from [41]).

This model can be succinctly described by the left-invariant vector field describing the motion of the needle tip in its body-fixed frame. The rigid body transformation

$$g = \begin{bmatrix} R & \mathbf{p} \\ \mathbf{0}^T & 1 \end{bmatrix} \in SE(3) \tag{3.1}$$

describes the orientation and position of the needle tip with respect to an inertial frame, where $R \in SO(3)$ and $\mathbf{d} \in \mathbb{R}^3$ are the rotation matrix and tip position respec-

tively. The velocities in the body fixed frame are given as

$$\Omega_{\text{tip}} = \left(g^{-1}\dot{g}\right)^{\vee} = V_1 v + V_2 \omega, \tag{3.2}$$

where the twists associated with needle insertion velocity and tip rotational velocity are $V_1 = \kappa e_3 + e_4$ and $V_2 = e_6$, where e_i, $i = 1, \ldots 6$ is the standard basis in $\mathbb{R}^6$. In most previous work on tip-steerable needles, it is assumed that the insertion and rotational velocities at base and tip were equal such that $v = u_1$ and $\omega = u_2$ where (u_1, u_2) are the control inputs to the needle insertion robot. However, we are twisting a long slender rod, so the rotation at the base is coupled to the rotation at the tip through a dynamical system describing needle torsion. The work done by Reed et al. [43] demonstrates the need for torsional dynamics compensation, but their solution for torsion compensation assumes that the needle remains a fixed length inside the tissue, an assumption clearly violated during continuous needle insertion. We build on Reed et al.'s result in the next section by incorporating the time-varying boundary conditions that result from continuous needle insertion.

3.2.2 Models of Time-Varying Torsional Dynamics

We present three different approaches to modeling the effects of torsional dynamics of tip-steerable needles. Each approach has advantages and disadvantages. All three methods utilize the modal techniques—the Fourier series decomposition and Galerkin

projection—to derive the equations of motions for the torsional dynamics. Figure 3.2 pictorially describes the three different modeling techniques. Figure 3.2(A) uses the time-varying modal dynamics formulation for the portion of the needle inside the tissue only. The rotation of the needle is controlled at the point where needle enters the tissue with zero internal torque on the portion outside the tissue. Figure 3.2(B) uses a single time-varying modal dynamics formulation for the entire length of the needle. We incorporate a unit step function to represent the boundary condition where viscous drag inside the tissue becomes "active". The rotation of the needle is controlled at the base of the needle. Figure 3.2(C) uses the time-varying modal dynamics formulation for the portion of the needle inside the tissue and an ideal torsional spring for the portion outside the tissue. The differences between each method is subtle; the modeling method identifies exactly what the torsional states represent and which control methods are admitted. Because of the subtleties, we present the complete derivation of each model even where some commonalities exist between the different models. Hereafter we will refer to each modeling technique as Model A, Model B, and Model C.

3.2.2.1   Model A: Rotational control at the tissue insertion point

Model A describes a system where we control the torque exerted at the point where the needle enters the tissue as shown in Figure 3.3. This assumes that the portion of the needle outside the tissue, behind the point of insertion, is able to rotate freely and
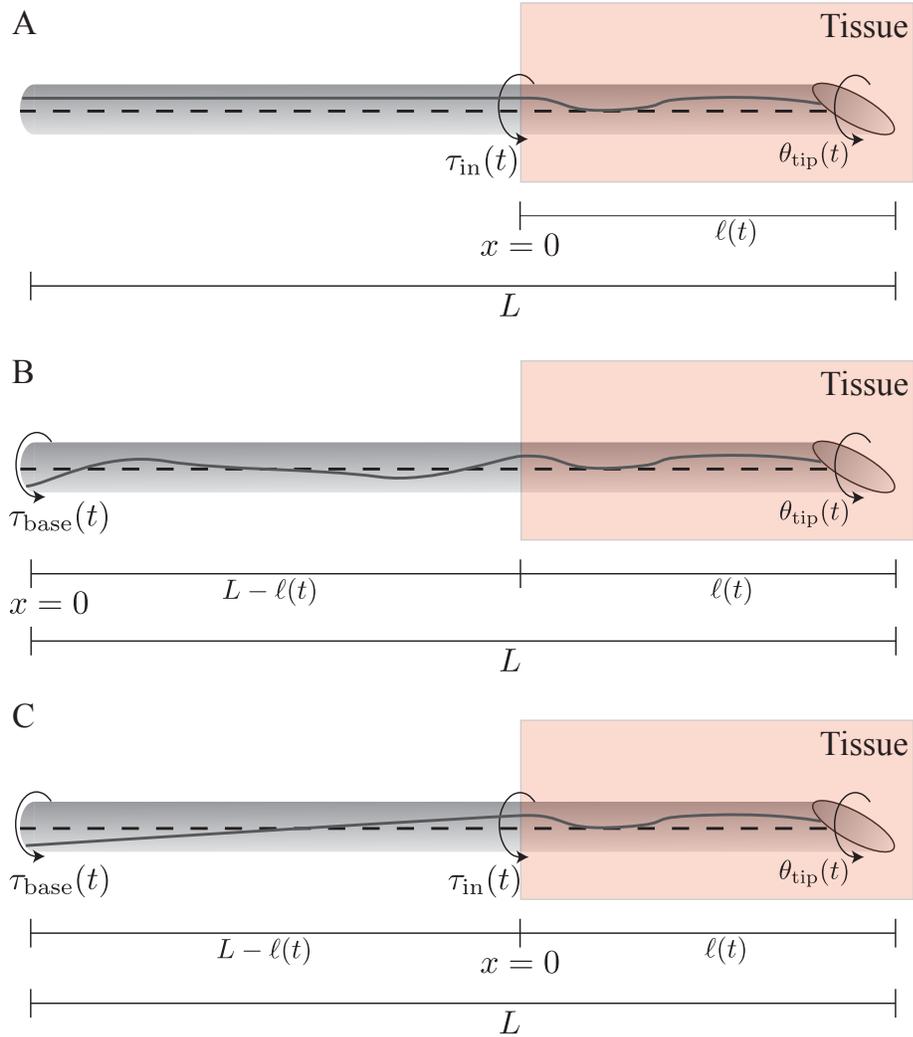
Figure 3.2: Three different models of the torsional dynamics of the needle. (A) We use the time-varying modal dynamics formulation for the portion of the needle inside the tissue only. The rotation of the needle is controlled at the point where needle enters the tissue with zero internal torque on the portion outside the tissue. (B) We use a single time-varying modal dynamics formulation for the entire length of the needle. We incorporate a unit step function to represent the boundary condition where viscous drag inside the tissue becomes "active". The rotation of the needle is controlled at the base of the needle. (C) We use the time-varying modal dynamics formulation for the portion of the needle inside the tissue and an ideal torsional spring for the portion outside the tissue. In all cases, there is a time-varying changing boundary condition as the needle is inserted. Here, the dashed line represents an imaginary line inscribed on the surface of the needle with zero torsion. The gray line indicates the same inscribed line while the needle is under torsion.

exerts no torque other than inertial effects. The inertial effects outside the tissues are negligible for small needles of relatively short lengths compared to the control torques and are ignored in the formulation. We model the portion inside the tissue using a partial differential equation (PDE) that incorporates the rotational inertial forces of the needle, viscous drag forces between needle and tissue, and the shear forces due to needle properties. This method allows the greatest degree of control over the orientation of the needle tip, when compared to the other methods described below. However, this requires a needle insertion robot that allows rotation control at the point of insertion. While this was attempted in earlier work by Webster et al. [50], the friction wheel design slipped too frequently to be an effective needle insertion mechanism. The robot used for the experiments shown in this dissertation does not admit this type of control. We present it here as the ideal control mechanism but only give simulation results.

Using the Newton-Euler formulation for an infinitesimal portion of the needle inside the tissue, Reed et al. [43] derived a PDE in $\theta(x,t)$ a function of space and time,

$$\eta\frac{\partial^2\theta}{\partial t^2} + \beta\frac{\partial\theta}{\partial t} - \kappa\frac{\partial^2\theta}{\partial x^2} = \delta(x)\tau_{\text{in}}(t), \tag{3.3}$$

where β represents viscous damping (assumed to be uniform along the needle shaft), and η is rotational inertia. Here, as in Reed et al.'s model, we assume that the external torque on the needle is applied at the point that the needle enters the tissue, which is incorporated mathematically via the product of a spatial Dirac impulse function,
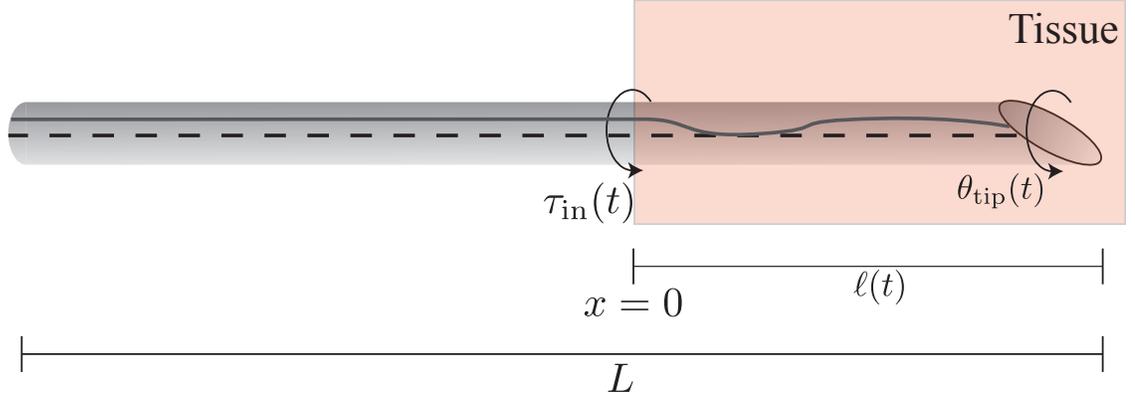
Figure 3.3: The torsional dynamics of the needle is modeled through Newton force formulation resulting in a partial differential equation solved via modal methods. There is a time-varying changing boundary condition as the needle is inserted. The needle is controlled via a torque exerted at the point where needle enters the tissue. Here, the dashed line represents an imaginary inscribed line with zero torsion. The gray line indicates the same inscribed line while the needle is under torsion.

$\delta(x)$, and the torque at the coupling between motor and the needle, $\tau_{\text{in}}(t)$.

Henceforth, our derivations deviate significantly from the previous work done by Reed et al. [43] in the following one key respect: we no longer model the system as a fixed length inside the tissue. Because the needle length inside the tissue is changing, we cannot make the assumption that the modal solution is separable in both space and time. Instead, we can only assume that the mode shapes are functions of both space and time and the mode coefficients are functions of time:

$$\theta(x,t) = \frac{1}{2}q_0(t) + \sum_{k=1}^{\infty} \psi_k(x,t)q_k(t) + \sum_{k=1}^{\infty} \phi_k(x,t)p_k(t) \qquad (3.4)$$

where

$$\left.\begin{aligned} \psi_j(x,t) &= \cos(\omega_j(t)x) \\[1em] \phi_j(x,t) &= \sin(\omega_j(t)x) \end{aligned}\right\}, \quad \text{and} \quad \omega_j(t) = \frac{j\pi}{\ell(t)}. \tag{3.5}$$

A common practice in solving PDEs is to find the infinite dimensional representation of the PDE using the assumed modal solution and projecting back onto the first n-modes [8, 49]. The technique taken in this chapter is one technique among a broader field of proper orthogonal decomposition and subsequent Galerkin projection [22, 45]. When the assumed solution is separable in space and time, where the mode shapes are function of the spatial variable and the mode coefficients are functions of time, the result of a Galerkin projection is guaranteed to be an ordinary differential equation (ODE) in time. This method of model order reduction is particularly apropos when the system has a viscous dissipative term causing exponential decay for states with high wavenumber, which our system satisfies.

For our system, the basis for the proper orthogonal decomposition are the torsional modes along the length of the needle inside the tissue as given in (3.5). As intimated previously, our system does not separate in space and time and we must perform the Galerkin projection and verify that each projection results in an ODE in time only; fortunately, the Galerkin projection for this system results in an ODE in time. To perform our Galerkin projection, we first substitute (3.4) into (3.3), and then project onto each mode shape. This rote computation is not included here in its entirety for brevity. We include a significant portion of this computation in the Appendix A

and Appendix B, including the Mathematica code listing to perform the complete computation. However, the properties of key importance for simplification during the computations are related to the orthogonality conditions for the mode shapes, as shown in (3.6).

$$\int_{-\ell(t)}^{\ell(t)} \psi_k(x,t)\phi_j(x_t)dx = 0 \quad \forall j,k > 0.$$

$$\int_{-\ell(t)}^{\ell(t)} \psi_k(x,t)\psi_j(x_t)dx = \begin{cases} 2\ell(t), j = k = 0, \\ \ell(t), j = k > 0, \\ 0, j \neq k. \end{cases}$$

$$\int_{-\ell(t)}^{\ell(t)} \psi_k(x,t)\psi_j(x_t)dx = \begin{cases} 0, j = k = 0, \\ \ell(t), j = k > 0, \\ 0, j \neq k. \end{cases}$$

(3.6)

The appropriate number of torsional modes to include in the truncated approximation of the system depends significantly on the tissue properties, needle properties, and control scheme employed. In Section 3.4, we compare and contrast through simulation and experimentation several model order truncations. Reed et al. analyzed a specific needle and tissue combination with experimentally computed damping and used Hankel singular values to determine an appropriate model order. The method of Hankel singular values requires the analytical computation of the state transition

matrix for the dynamical system—a computation we have not achieved yet for this now time-varying system. For a general n-th order projection, the resulting ODE is of the form

$$\begin{bmatrix} M_1 & 0 \\ 0 & M_2 \end{bmatrix} \begin{bmatrix} \ddot{\mathbf{q}} \\ \ddot{\mathbf{p}} \end{bmatrix} + \begin{bmatrix} D_1 & 0 \\ 0 & D_2 \end{bmatrix} \begin{bmatrix} \dot{\mathbf{q}} \\ \dot{\mathbf{p}} \end{bmatrix} + \begin{bmatrix} K_1 & 0 \\ 0 & K_2 \end{bmatrix} \begin{bmatrix} \mathbf{q} \\ \mathbf{p} \end{bmatrix} = \begin{bmatrix} P \\ 0 \end{bmatrix} \tau_{\text{in}}, \qquad (3.7)$$

where the vectors $\mathbf{q}$ and $\mathbf{p}$ are the time-varying coefficients to the cosine and sine modes, respectively, as shown in (3.4).

We first note that the cosine and sine modes are decoupled, the sine modes are unforced, and the sine modes are naturally asymptotically stable. Thus, we can assume that for any experiment the sine modes are initially unexcited and can never be excited. From this point forward we will disregard the sine modes as both uncontrollable and always zero; the full torsional dynamics from insertion point to tip with only cosine terms is

$$M_1\ddot{\mathbf{q}} + D_1\dot{\mathbf{q}} + K_1\mathbf{q} = P\tau_{\text{in}}(t). \qquad (3.8)$$

Torque control

We also note that the inertial forces associated with this system are quite small compared to the damping, shear, and control forces such that we can simplify the system to a coupled first order system by neglecting the inertial effects,

$$\dot{\mathbf{q}} = \underbrace{-D_1^{-1}K_1}_{A(t)}\mathbf{q} + \underbrace{D^{-1}P}_{B(t)}\tau_{\text{in}}(t). \qquad (3.9)$$

Notice also that the velocity at the tip of the needle in the torsional dynamics, $\dot{\theta}(x, t)$, is equal to the body fixed rotational velocity, ω, given in (3.2). Thus, we compute

$$\theta_{\text{tip}} = \theta(x, t)|_{x=\ell(t)} \approx \frac{1}{2} q_0 + \sum_{k=1}^{n} \psi(\ell(t), t) q_k(t) = \underbrace{\begin{bmatrix} \frac{1}{2} & -1 & 1 & \cdots & (-1)^{n-1} \end{bmatrix}}_{C_\ell} \mathbf{q} \quad (3.10)$$

and differentiate this to obtain

$$\omega = \dot{\theta}_{\text{tip}} = C_\ell \dot{\mathbf{q}} = \underbrace{C_\ell A(t)}_{C(t)} \mathbf{q} + \underbrace{C_\ell B(t)}_{D(t)} \tau_{\text{in}}(t),$$

such that the final system can be written in a familiar linear, time-varying form:

$$\dot{\mathbf{q}} = A(t)\mathbf{q} + B(t)\tau_{\text{in}}(t)$$

$$\omega = C(t)\mathbf{q} + D(t)\tau_{\text{in}}(t). \qquad (3.11)$$

Velocity control

Often, we desire to implement a controller that does not rely on a torque sensor. Torque sensors are often inaccurate or noisy, fragile, and expensive. When a torque sensor is not used, the dynamics given in (3.11) cannot be used to close the loop in a feedback implementation. Thus, we work to find the algebraic relationship between velocities applied at the insertion point to the applied torque and states of the system.

First, we assume that we can accurately control and measure the velocity of the needle at the point of insertion. Then, we can rewrite the time derivative of assumed

solution to the PDE, evaluated at the insertion point, as

$$\dot{\theta}(0,t) = \dot{\theta}_{\text{in}}(t) = -C_0 D_1^{-1} K_1 \mathbf{q} - C_0 D_1^{-1} P \tau_{\text{in}}(t) \tag{3.12}$$

where $\dot{\theta}_{\text{in}}(t)$ is the controlled velocity at the base of the needle. We now solve for

the torque at the insertion point in terms of the state of the system and the velocity

input,

$$C_0 D_1^{-1} P \tau_{\text{in}}(t) + C_0 D_1^{-1} K \mathbf{q} = -\dot{\theta}_{\text{in}}(t)$$

$$C_0 D_1^{-1} P \tau_{\text{in}}(t) = -C_0 D_1^{-1} K_1 \mathbf{q} - \dot{\theta}_{\text{in}}(t) \tag{3.13}$$

$$\tau_{\text{in}}(t) = \frac{1}{C_0 D_1^{-1} P} \left(-C_0 D_1^{-1} K_1 \mathbf{q} - \dot{\theta}_{\text{in}}(t) \right)$$

Plugging this torque constraint back into the original dynamical equation (3.11) we

find a modified form of the system where the control input is now the velocity at the

insertion point.

$$\dot{q} = -D_1^{-1} K_1 \mathbf{q} + -D_1^{-1} P \tau_{\text{in}}(t)$$

$$= -D_1^{-1} K_1 \mathbf{q} + -D_1^{-1} P \left[\frac{1}{C_0 D_1^{-1} P} \left(-C_0 D_1^{-1} K_1 \mathbf{q} - \dot{\theta}_{\text{in}}(t) \right) \right] \tag{3.14}$$

$$= \underbrace{\left(\frac{1}{C_0 D_1^{-1} P} D_1^{-1} P C_0 D_1^{-1} K_1 - D_1^{-1} K_1 \right)}_{A(t)} \mathbf{q} + \underbrace{\frac{1}{C_0 D_1^{-1} P} D_1^{-1} P \dot{\theta}_{\text{in}}(t)}_{B(t)}$$

From this form we can show that we no longer need to incorporate the state q_0 into

this system of dynamical equations. This is seen in two ways:

1. The structure of the matrix K_1 causes the system to always have an eigenvector of e_1 with eigenvalue 0. This means that the state q_0 has no effect on the vector field $(q, \dot{q})$.

2. The boundary conditions also show that both q_0 and $\dot{q}_0$ can be computed from the values of $\{q_k\}$ and $\{\dot{q}_k\}$, respectively.

This further reduction of state will become critical when incorporating the torsional dynamics into the kinematic model of tip-steerable needles to avoid problems with observability and non-minimal realization. We see the relationship between $\dot{q}_0$ and the rest of the velocities by examining the boundary conditions.

$$
\begin{aligned}
\theta_{\text{in}}(t) = \theta(0, t) = \frac{1}{2}q_0 + \sum_{k=1}^{n} q_k \Rightarrow q_0 = 2\left(\theta_{\text{in}}(t) - \sum_{k=1}^{n} q_k\right) \\
\dot{\theta}_{\text{in}}(t) = \dot{\theta}(0, t) = \frac{1}{2}\dot{q}_0 + \sum_{k=1}^{n} \dot{q}_k \Rightarrow \dot{q}_0 = 2\left(\dot{\theta}_{\text{in}}(t) - \sum_{k=1}^{n} \dot{q}_k\right)
\end{aligned}
\tag{3.15}
$$

The angle at the needle insertion point, $\theta_{\text{in}}(t)$, can be measured with an encoder and thus the DC mode coefficient can be recovered from the encoder measurement and the rest of the states $\{q_i\}$.

$$
\begin{aligned}
\omega = \dot{\theta}_{\text{tip}} &= \frac{1}{2}\dot{q}_0 + \sum_{k=1}^{n}(-1)^k \dot{q}_k \\
&= \left(\dot{\theta}_{\text{in}}(t) - \sum_{k=1}^{n}\dot{q}_k\right) + \sum_{k=1}^{n}(-1)^k \dot{q}_k \\
&= \underbrace{\begin{bmatrix} -2 & 0 & -2 & 0 & \cdots & -2 \end{bmatrix}}_{C_l} \begin{bmatrix} \dot{q}_1 \\ \dot{q}_2 \\ \dot{q}_3 \\ \dot{q}_4 \\ \cdots \\ \dot{q}_n \end{bmatrix} + \dot{\theta}_{\text{in}}(t) \\
&= \underbrace{C_\ell A(t)}_{C(t)}\mathbf{q} + \underbrace{(1 + C_\ell B(t))}_{D(t)}\dot{\theta}_{\text{in}}(t)
\end{aligned}
\tag{3.16}
$$

Now that the rotational velocity at the tip of the needle is independent of the DC mode coefficient, which will be the rotational velocity input into the tip-steerable needle kinematics, we can reduce the dimension of the state equations for the torsional dynamics to disregard the dynamics associated with the DC mode. This reduction of state is written as

$$
\dot{\mathbf{q}} = \underbrace{\left[\frac{1}{C_0 D^{-1} P} D^{-1} P C_0 D^{-1} K - D^{-1} K\right]_{(2\cdots n, 2\cdots n)}}_{A(t)} \mathbf{q} + \underbrace{\left[\frac{1}{C_0 D^{-1} P} D^{-1} P\right]_{(2\cdots n)}}_{B(t)} \dot{\theta}_{\text{in}}(t)
\tag{3.17}
$$

where $[\ ]_{(2\cdots n, 2\cdots n)}$ represents the principal submatrix with the first row and column eliminated and $[\ ]_{(2\cdots n)}$ represents the vector with the first element removed. From

this point forward, when we use this model we use the vector $\mathbf{q}$ to represent the mode coefficients, understanding that this represents the reduced state vector. The reduction also eliminates the zero eigenvalue of the torsional dynamics.

Now, we combine (3.16) and (3.17) to get the full torsional dynamics and associated output,

$$\dot{\mathbf{q}} = A(t)\mathbf{q} + B(t)\dot{\theta}_{\text{in}}(t)$$
$$\omega = C(t)\mathbf{q} + D(t)\dot{\theta}_{\text{in}}(t). \tag{3.18}$$

Discussion

Here it is important to recognize that the dynamics structure represented by $A(t)$, $B(t)$, $C(t)$, and $D(t)$ in (3.11) and (3.18) differ considerably. We overloaded this use of notation here so the discussion of combining the torsional dynamics with the tip-steerable needle kinematics and subsequent control, discussed in Sections 3.2.3 and 3.3, can be presented generically given either of these dynamics structures or the dynamics structures given for Model B and Model C.

3.2.2.2 Model B: Rotational control at the needle base with step function damping

Model B describes a system where we control the torque exerted at the base of the needle as shown in Figure 3.4. We model the entire needle using a single partial differential equation (PDE) that incorporates the rotational inertial forces of the needle, viscous drag forces between needle and tissue, and the shear forces
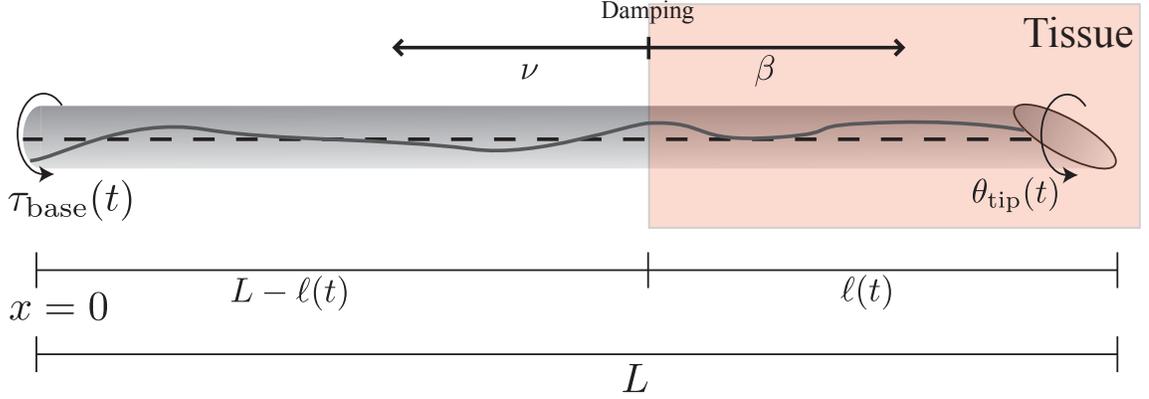
Figure 3.4: The torsional dynamics of the entire needle is modeled through a single Newton force formulation resulting in a partial differential equation. There is a time-varying changing boundary condition as the needle is inserted where the damping on either side of the boundary condition differs. Here we make the damping outside the tissue non-zero, but very small, to provide a greater degree of numerical stability in implementation. The PDE is solved via modal methods. The dashed line represents an imaginary inscribed line with zero torsion. The gray line indicates the same inscribed line while the needle is under torsion.

due to needle properties. In this model, there is a time-varying boundary condition separating the portions on the needle inside the tissue and the portion outside—the damping forces differ inside and outside the tissue.

Using the Newton-Euler formulation for an infinitesimal portion of the needle inside the tissue, Reed et al. [43] derived a PDE in $\theta(x,t)$ a function of space and time. We modify this formulation to include two differing damping values for the portion inside the tissue and the portion outside the tissue,

$$\eta\frac{\partial^2\theta}{\partial t^2} + (h(x - (L - \ell(t)))\beta + (1 - h(x - (L - \ell(t))))\nu)\frac{\partial\theta}{\partial t} - \kappa\frac{\partial^2\theta}{\partial x^2} = \delta(x)\tau_{\text{base}}(t),$$

$$(3.19)$$

where β represents viscous damping inside the tissue (assumed to be uniform along the needle shaft), ν represents the damping outside the tissue (assumed to be nearly negligible), η is rotational inertia, and $h(\,\cdot\,)$ is the unit step function. The external torque on the needle is applied at the base of the needle, which is incorporated mathematically via the product of a spatial Dirac impulse function, $\delta(x)$, and the torque at the coupling between motor and the needle, $\tau_{\text{base}}(t)$.

While theoretically there is no reason for there to be damping for the portion of the needle outside the tissue in a perfect system, we include this term for two reasons: (1) heat generated through oscillating, air drag, and other effects will eventually dampen any oscillations in the portion outside the tissue and (2) including this term prevent problems of numerical ill-conditioning in the final system equations when the needle is only a short distance inside the tissue. Henceforth, our derivations deviate significantly from the previous work done by Reed et al. [43] in the following two key respects: (1) we no longer model the system as a fixed length inside the tissue and (2) we do not assume torque control at the point the needle enters the tissue.

As done in Model A, we solve this PDE by finding the infinite dimensional solution to the PDE using the assumed modal solution and projecting back onto the first n modes [8, 49]. For our system, the basis for the proper orthogonal decomposition are the torsional modes along the length of the needle as given in (3.21). Because the needle length inside the tissue is changing, we cannot make the assumption that the modal solution is separable in both space and time. Instead, we can only assume that

the mode shapes are functions of both space and time and the mode coefficients are functions of time:

$$\theta(x,t) = \frac{1}{2}q_0(t) + \sum_{k=1}^{\infty}\psi_k(x)q_k(t) + \sum_{k=1}^{\infty}\phi_k(x)p_k(t) \tag{3.20}$$

where

$$\left.\begin{array}{l}\psi_j(x) = \cos(\omega_j x) \\[2mm] \phi_j(x) = \sin(\omega_j x)\end{array}\right\}, \quad \text{and} \quad \omega_j = \frac{j\pi}{L}. \tag{3.21}$$

As in the Reed et al. model, this assumed solution is separable in space and time and the Galerkin projection will result in an ODE in time only. Because the mode shapes are defined over the entire length of the needle, there is no spatial component to the length of the modes. However, the boundary condition—the boundary between the damping inside and outside the tissue—causes the resulting system of ordinary differential equations to be a linear time-varying system.

To perform our Galerkin projection, we first substitute (3.20) into (3.19), and then project onto each mode shape. We include a significant portion of the computation for Model B in Appendix A. Appendix B includes a Mathematica code listing to perform the complete computation for Model B. For a general n-th order projection, the resulting ODE is of the form

$$\begin{bmatrix} M_1 & 0 \\ 0 & M_2 \end{bmatrix}\begin{bmatrix} \ddot{\mathbf{q}} \\ \ddot{\mathbf{p}} \end{bmatrix} + \begin{bmatrix} D_1 & 0 \\ 0 & D_2 \end{bmatrix}\begin{bmatrix} \dot{\mathbf{q}} \\ \dot{\mathbf{p}} \end{bmatrix} + \begin{bmatrix} K_1 & 0 \\ 0 & K_2 \end{bmatrix}\begin{bmatrix} \mathbf{q} \\ \mathbf{p} \end{bmatrix} = \begin{bmatrix} P \\ 0 \end{bmatrix}\tau_{\text{base}}, \tag{3.22}$$

where the vectors $\mathbf{q}$ and $\mathbf{p}$ are the time-varying coefficients to the cosine and sine

modes, respectively, as shown in (3.20). As in Model A, the cosine and sine modes are decoupled, the sine modes are unforced, and the sine modes are naturally asymptotically stable. Thus, we can assume that for any experiment the sine modes are initially unexcited and can never be excited. From this point forward we will disregard the sine modes as both uncontrollable and always zero; the full torsional dynamics from base to tip with only cosine terms is

$$M_1 \ddot{\mathbf{q}} + D_1 \dot{\mathbf{q}} + K_1 \mathbf{q} = P \tau_{\text{base}}(t). \tag{3.23}$$

Torque control

We also note that the inertial forces associated with this system are quite small compared to the damping, shear, and control forces such that we can simplify the system to a coupled first order system by neglecting the inertial effects,

$$\dot{\mathbf{q}} = \underbrace{-D_1^{-1} K_1}_{A(t)} \mathbf{q} + \underbrace{D^{-1} Pt}_{B(t)} \tau_{\text{base}}(t). \tag{3.24}$$

Notice also that the velocity at the tip of the needle in the torsional dynamics, $\dot{\theta}(x,t)$, is equal to the body fixed rotational velocity, ω, given in equation (3.2). Thus, we compute

$$\theta_{\text{tip}} = \theta(x,t)|_{x=\ell(t)} \approx \frac{1}{2} q_0 + \sum_{k=1}^{n} \psi(\ell(t),t) q_k(t) = \underbrace{\begin{bmatrix} \frac{1}{2} & -1 & 1 & \cdots & (-1)^{n-1} \end{bmatrix}}_{C_\ell} \mathbf{q} \tag{3.25}$$

and differentiate this to obtain

$$\omega = \dot{\theta}_{\text{tip}} = C_\ell \dot{\mathbf{q}} = \underbrace{C_\ell A(t)}_{C(t)} \mathbf{q} + \underbrace{C_\ell B(t)}_{D(t)} \tau_{\text{base}}(t),$$

such that the final system can be written in a familiar linear, time-varying form:

$$\dot{\mathbf{q}} = A(t)\mathbf{q} + B(t)\tau_{\text{base}}(t)$$

$$\omega = C(t)\mathbf{q} + D(t)\tau_{\text{base}}(t). \tag{3.26}$$

Velocity control

Often, we desire to implement a controller that does not rely on a torque sensor. Torque sensors are often inaccurate or noisy, fragile, and expensive. When a torque sensor is not used, the dynamics given in (3.26) cannot be used to close the loop in a feedback implementation. Thus, we work to find the algebraic relationship between velocities applied at the insertion point to the applied torque and states of the system.

First, we assume that we can accurately control and measure the velocity of the needle at the point of insertion. Then, we can rewrite the time derivative of assumed solution to the PDE, evaluated at the insertion point, as

$$\dot{\theta}(0, t) = \dot{\theta}_{\text{base}}(t) = -C_0 D_1^{-1} K_1 \mathbf{q} - C_0 D_1^{-1} P \tau_{\text{base}}(t) \tag{3.27}$$

where $\dot{\theta}_{\text{in}}(t)$ is the controlled velocity at the base of the needle. We now solve for

the torque at the insertion point in terms of the state of the system and the velocity input,

$$C_0 D_1^{-1} P \tau_{\text{base}}(t) + C_0 D_1^{-1} K \mathbf{q} = -\dot{\theta}_{\text{base}}(t)$$

$$\tau_{\text{base}}(t) = \frac{1}{C_0 D_1^{-1} P} \left(-C_0 D_1^{-1} K_1 \mathbf{q} - \dot{\theta}_{\text{base}}(t) \right) \tag{3.28}$$

Plugging this torque constraint back into the original dynamical equation (3.26) we find a modified form of the system where the control input is now the velocity at the insertion point.

$$
\begin{aligned}
\dot{q} &= -D_1^{-1} K_1 \mathbf{q} + -D_1^{-1} P \tau_{\text{base}}(t) \\
&= -D_1^{-1} K_1 \mathbf{q} + -D_1^{-1} P \left[\frac{1}{C_0 D_1^{-1} P} \left(-C_0 D_1^{-1} K_1 \mathbf{q} - \dot{\theta}_{\text{base}}(t) \right) \right] \\
&= \underbrace{\left(\frac{1}{C_0 D_1^{-1} P} D_1^{-1} P C_0 D_1^{-1} K_1 - D_1^{-1} K_1 \right)}_{A(t)} \mathbf{q} + \underbrace{\frac{1}{C_0 D_1^{-1} P} D_1^{-1} P}_{B(t)} \dot{\theta}_{\text{base}}(t)
\end{aligned} \tag{3.29}
$$

From this form we can show that we no longer need to incorporate the state q_0 into this system of dynamical equations. This is seen in two ways:

1. The structure of the matrix K_1 causes the system to always have an eigenvector of e_1 with eigenvalue 0. This means that the state q_0 has no effect on the vector field $(q, \dot{q})$.

2. The boundary conditions also show that both q_0 and $\dot{q}_0$ can be computed from the values of $\{q_k\}$ and $\{\dot{q}k\}$ respectively.

This further reduction of state will become critical when incorporating the torsional dynamics into the kinematic model of tip-steerable needles to avoid problems with observability and non-minimal realization. We see the relationship between $\dot{q}_0$ and the rest of the velocities by examining the boundary conditions.

$$
\begin{aligned}
\theta_{\text{base}}(t) = \theta(0, t) &= \frac{1}{2}q_0 + \sum_{k=1}^{n} q_k \Rightarrow q_0 = 2\left(\theta_{\text{base}}(t) - \sum_{k=1}^{n} q_k\right) \\
\dot{\theta}_{\text{base}}(t) = \dot{\theta}(0, t) &= \frac{1}{2}\dot{q}_0 + \sum_{k=1}^{n} \dot{q}_k \Rightarrow \dot{q}_0 = 2\left(\dot{\theta}_{\text{in}}(t) - \sum_{k=1}^{n} \dot{q}_k\right)
\end{aligned}
\tag{3.30}
$$

The angle at the base of the needle, $\theta_{\text{base}}(t)$, can be measured with an encoder and thus the DC mode coefficient can be recovered from the encoder measurement and the rest of the states $\{q_i\}$.

$$\omega = \dot{\theta}_{\text{tip}} = \frac{1}{2}\dot{q}_0 + \sum_{k=1}^{n}(-1)^k\dot{q}_k$$

$$= \left(\dot{\theta}_{\text{base}}(t) - \sum_{k=1}^{n}\dot{q}_k\right) + \sum_{k=1}^{n}(-1)^k\dot{q}_k$$

$$= \underbrace{\begin{bmatrix} -2 & 0 & -2 & 0 & \cdots & -2 \end{bmatrix}}_{C_l} \begin{bmatrix} \dot{q}_1 \\ \dot{q}_2 \\ \dot{q}_3 \\ \dot{q}_4 \\ \cdots \\ \dot{q}_n \end{bmatrix} + \dot{\theta}_{\text{base}}(t) \tag{3.31}$$

$$= \underbrace{C_\ell A(t)}_{C(t)}\mathbf{q} + \underbrace{(1 + C_\ell B(t))}_{D(t)}\dot{\theta}_{\text{base}}(t)$$

Now that the rotational velocity at the tip of the needle is independent of the DC mode coefficient, which will be the rotational velocity input into the tip-steerable needle kinematics, we can reduce the dimension of the state equations for the torsional dynamics to disregard the dynamics associated with the DC mode. This reduction of state is written as

$$\dot{\mathbf{q}} = \underbrace{\left[\frac{1}{C_0 D^{-1}P}D^{-1}PC_0 D^{-1}K - D^{-1}K\right]_{(2\cdots n,2\cdots n)}}_{A(t)}\mathbf{q} + \underbrace{\left[\frac{1}{C_0 D^{-1}P}D^{-1}P\right]_{(2\cdots n)}}_{B(t)}\dot{\theta}_{\text{in}}(t)$$

$$\tag{3.32}$$

where $[\ ]_{(2\cdots n,2\cdots n)}$ represents the principal submatrix with the first row and column eliminated and $[\ ]_{(2\cdots n)}$ represents the vector with the first element removed. From this

point forward, when we use this model and control method the vector $\mathbf{q}$ to represent the mode coefficients, understand that this represents the reduced state vector. The reduction also eliminates the zero eigenvalue of the torsional dynamics.

Now, we combine (3.31) and (3.32) to get the full torsional dynamics and associated output,

$$\dot{\mathbf{q}} = A(t)\mathbf{q} + B(t)\dot{\theta}_{\text{in}}(t)$$

$$\omega = C(t)\mathbf{q} + D(t)\dot{\theta}_{\text{in}}(t). \tag{3.33}$$

3.2.2.3 Model C: Rotational control at the needle base with an ideal torsional spring outside the tissue

Model C of continuous needle insertion accounts for torsion both inside and outside the tissue as shown in Figure 3.5. We model the portion inside the tissue using a partial differential equation (PDE) that incorporates the rotational inertial forces of the needle, viscous drag forces between needle and tissues, and the shear forces due to needle properties. We model the portion outside the tissue as an ideal torsional spring whose spring constant is a function of the polar moment of inertia, J, the needle shear modulus, G, and the length outside the tissue, $L - l(t)$.

Using the Newton-Euler formulation for an infinitesimal portion of the needle inside the tissue, Reed et al. [43] derived a PDE in $\theta(x, t)$ a function of space and time,

$$\eta \frac{\partial^2 \theta}{\partial t^2} + \beta \frac{\partial \theta}{\partial t} - \kappa \frac{\partial^2 \theta}{\partial x^2} = \delta(x)\tau_{\text{in}}(t), \tag{3.34}$$
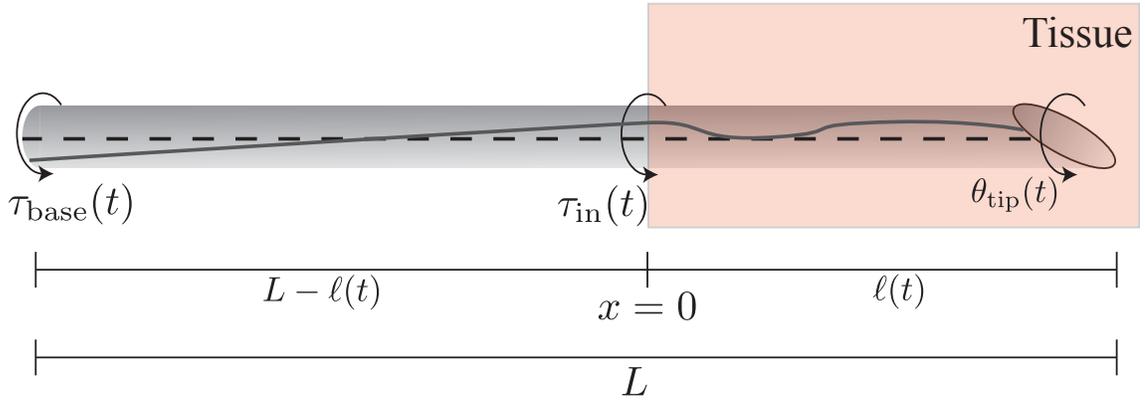
Figure 3.5: The torsional dynamics of the needle is divided into the portion inside the tissue outside the tissue. There is a time-varying changing boundary condition as the needle is inserted. The portion inside the needle is modeled through Newton force formulation resulting in a partial differential equation solved via modal methods. The portion outside the tissue is modeled as a torsional spring. Here, the dashed line represents an imaginary inscribed line with zero torsion. The gray line indicates the same inscribed line while the needle is under torsion.

where β represents viscous damping (assumed to be uniform along the needle shaft), and η is rotational inertia. In Reed et al.'s model, it is assumed that the external torque on the needle is applied at the point that the needle enters the tissue, which is incorporated mathematically via the product of a spatial Dirac impulse function, $\delta(x)$, and the torque at the coupling between motor and the needle, $\tau_{\text{in}}(t)$.

Henceforth, our derivations deviate significantly from the previous work done by Reed et al. [43] in the following two key respects: (1) we no longer model the system as a fixed length inside the tissue and (2) we do not assume torque control at the point the needle enters the tissue.

First, we note that the torque at the motor–needle interface is exactly the same as

the torque at the tissue boundary, i.e. $\tau_{\text{in}} = \tau_{\text{base}}$, since we assume an ideal torsional spring for the portion of the needle outside the tissue. Hence, for the portion of the needle *inside* the tissue, we can still adopt the formulation in (3.34), where the spatial impulse is taken at $x = 0$. In other words, the torsional angle of the needle at the point of insertion into the tissue can be different from the angle at the motor, but the torque is the same all along the portion of the needle outside the tissue.

Because the needle length inside the tissue is changing, we cannot make the assumption that the modal solution is separable in both space and time. Instead, we can only assume that the mode shapes are functions of both space and time and the mode coefficients are functions of time:

$$\theta(x,t) = \frac{1}{2}q_0(t) + \sum_{k=1}^{\infty} \psi_k(x,t)q_k(t) + \sum_{k=1}^{\infty} \phi_k(x,t)p_k(t) \tag{3.35}$$

where

$$\left.\begin{array}{l} \psi_j(x,t) = \cos(\omega_j(t)x) \\[2mm] \phi_j(x,t) = \sin(\omega_j(t)x) \end{array}\right\}, \quad \text{and} \quad \omega_j(t) = \frac{j\pi}{\ell(t)}. \tag{3.36}$$

As with the two previous models, the basis for the proper orthogonal decomposition are the torsional modes along the length of the needle as given in (3.36). As before, our system does not separate in space and time and we must perform the Galerkin projection and verify that each projection results in an ODE in time only; fortunately, the Galerkin projection for this system results in such. To perform our Galerkin

projection, we first substitute (3.35) into (3.34), and then project onto each mode shape. This rote computation is not included here in its entirety for brevity. We include a significant portion of this computation in the Appendix A and Appendix B, including the Mathematica code listing to perform the complete computation. However, the properties of key importance for simplification during the computations are related to the orthogonality conditions for the mode shapes, as shown in (3.37).

$$\int_{-\ell(t)}^{\ell(t)} \psi_k(x,t)\phi_j(x_t)dx = 0 \quad \forall j,k > 0.$$

$$\int_{-\ell(t)}^{\ell(t)} \psi_k(x,t)\psi_j(x_t)dx = \begin{cases} 2\ell(t), j = k = 0, \\ \ell(t), j = k > 0, \\ 0, j \neq k. \end{cases}$$

$$\int_{-\ell(t)}^{\ell(t)} \psi_k(x,t)\psi_j(x_t)dx = \begin{cases} 0, j = k = 0, \\ \ell(t), j = k > 0, \\ 0, j \neq k. \end{cases}$$

(3.37)

The appropriate number of torsional modes to include in the truncated approximation of the system depends significantly on the tissue properties, needle properties, and control scheme employed. In Section 3.4, we compare and contrast through simulation and experiments several model order truncations. Reed et al. analyzed a specific needle and tissue combination with experimentally computed damping and

used Hankel singular values to determine an appropriate model order. For a general n-th order projection, the resulting ODE is of the form

$$
\begin{bmatrix} M_1 & 0 \\ 0 & M_2 \end{bmatrix} \begin{bmatrix} \ddot{\mathbf{q}} \\ \ddot{\mathbf{p}} \end{bmatrix} + \begin{bmatrix} D_1 & 0 \\ 0 & D_2 \end{bmatrix} \begin{bmatrix} \dot{\mathbf{q}} \\ \dot{\mathbf{p}} \end{bmatrix} + \begin{bmatrix} K_1 & 0 \\ 0 & K_2 \end{bmatrix} \begin{bmatrix} \mathbf{q} \\ \mathbf{p} \end{bmatrix} = \begin{bmatrix} P \\ 0 \end{bmatrix} \tau_{\text{in}}, \tag{3.38}
$$

where the vectors $\mathbf{q}$ and $\mathbf{p}$ are the time-varying coefficients to the cosine and sine modes, respectively, as shown in (3.35).

We first note that the cosine and sine modes are decoupled, the sine modes are unforced, and the sine modes are naturally asymptotically stable. Thus, we can assume that for any experiment the sine modes are initially unexcited and can never be excited. From this point forward we will disregard the sine modes as both uncontrollable and always zero.

We model the portion of the needle outside the tissue as an ideal torsional spring, namely

$$
\theta_{\text{base}} - \theta_{\text{in}} = \tau_{\text{in}}(t) \frac{L - \ell(t)}{JG}. \tag{3.39}
$$

Here the position of at the insertion point of the needle, θ_{in}, is written in terms of the mode shapes and mode coefficients:

$$
\begin{aligned}
\theta_{\text{in}} = \theta(x, t)|_{x=0} &\approx \frac{1}{2} q_0 + \sum_{k=1}^{n} \psi(0, t) q_k(t) \\
&= \underbrace{\begin{bmatrix} \frac{1}{2} & 1 & \cdots & 1 \end{bmatrix}}_{C_0} \mathbf{q}.
\end{aligned} \tag{3.40}
$$

The torque resulting from the rotational position at the base of the needle and the modal representation of the rotational position at the insertion is

$$\tau_{\text{in}} = -\frac{JG}{L - \ell(t)} C_0 \mathbf{q} + \frac{JG}{L - \ell(t)} \theta_{\text{base}}, \tag{3.41}$$

where θ_{base} is the control input for subsequent control computations. The term $\frac{JG}{L-\ell(t)}$ can be thought of as the time-varying, lumped-parameter spring constant for the portion of the needle outside the tissue.

Substituting the torque constraint from (3.41) into the ODE representing the torsional dynamics inside the tissue in (3.38) and neglecting the sinusoidal modes, the full torsional dynamics from base to tip is

$$M_1 \ddot{\mathbf{q}} + D_1 \dot{\mathbf{q}} + \left(K_1 + \frac{JG}{L - \ell(t)} PC_0 \right) \mathbf{q} = \frac{JG}{L - \ell(t)} P\theta_{\text{base}}. \tag{3.42}$$

We also note that the inertial forces associated with this system are quite small compared to the damping, shear, and control forces such that we can simplify the system to a coupled first order system,

$$\dot{\mathbf{q}} = \underbrace{-D_1^{-1} \left(K_1 + \frac{JG}{L - \ell(t)} PC_0 \right)}_{A(t)} \mathbf{q} + \underbrace{D^{-1} \frac{JG}{L - \ell(t)} P}_{B(t)} \theta_{\text{base}}. \tag{3.43}$$

Notice also that the velocity at the tip of the needle in the torsional dynamics, $\dot{\theta}(x,t)$, is equal to the body fixed rotational velocity, ω, given in equation (3.2). Thus, we

compute

$$\theta_{\text{tip}} = \theta(x,t)|_{x=\ell(t)} \approx \frac{1}{2}q_0 + \sum_{k=1}^{n} \psi(l(t),t)q_k(t) = \underbrace{\left[\frac{1}{2} \quad -1 \quad 1 \quad \cdots \quad (-1)^{n-1}\right]}_{C_\ell} \mathbf{q} \quad (3.44)$$

and differentiate this to obtain

$$\omega = \dot{\theta}_{\text{tip}} = C_\ell \dot{\mathbf{q}} = \underbrace{C_\ell A(t)}_{C(t)} \mathbf{q} + \underbrace{C_\ell B(t)}_{D(t)} \theta_{\text{base}},$$

such that the final system can be written in a familiar linear, time-varying form:

$$\dot{\mathbf{q}} = A(t)\mathbf{q} + B(t)\theta_{\text{base}}$$

$$\omega = C(t)\mathbf{q} + D(t)\theta_{\text{base}}. \tag{3.45}$$

Here, in contrast to Model A and Model B, there is only one control method. Because we model the portion of the needle outside the tissue as an ideal torsional spring, torque control does not make sense. If we could instantaneously exert a torque at the base of the needle, this modeling method would be identical mathematically to Model A because the torque along the entire length of the needle outside the tissue is equivalent. However, that is not the case. This model uses the ideal spring model to exert a torque at the insertion point base on the relative angle between the base and the insertion point. To implement a controller that closes the loop around torque with this model including the ideal torsional spring, we would also need a full

characterization of the motor and gear train dynamics.

3.2.3   Integration: Full Needle Dynamics

In the previous sections, we presented three different models to represent the torsional dynamics of tip-steerable needles. Some of the models also had variations with a modified control input leading to five distinct representations of the torsional dynamics. The one commonality between all the models was that the output of the model was the rotation of the needle in the body-fixed frame of the tip of the needle. That is, each of the model can be written of the form

$$\dot{\mathbf{q}} = A(t)\mathbf{q} + B(t)u$$
$$\omega = C(t)\mathbf{q} + D(t)u$$

(3.46)

if $A(t), B(t), C(t), D(t)$, and u are identified with the appropriate model being used. Table 3.1 gives an overview of the models, matrices, and control inputs coming from (3.11), (3.18), (3.26), (3.33), and (3.45).

We now couple the torsional dynamics with the existing kinematic model. The velocity at the tip of the needle in the torsional dynamics, $\dot{\theta}(x,t)$, is equal to the body fixed rotational velocity, ω, given in equation (3.46). The full coupled form of

Model (*variation*)	Dynamics Equations	Control (u)
PDE for needle inside tissue (*torque control at the insertion point*)	Equation 3.11	$u = \tau_{\text{in}}(t)$
PDE for needle inside tissue (*velocity control at the insertion point*)	Equation 3.18	$u = \dot{\theta}_{\text{in}}(t)$
PDE for entire needle with step damping (*torque control at the needle base*)	Equation 3.26	$u = \tau_{\text{base}}(t)$
PDE for entire needle with step damping (*velocity control at the needle base*)	Equation 3.33	$u = \dot{\theta}_{\text{base}}(t)$
PDE for needle inside tissue, ideal spring for outside tissue (*position control at the needle base*)	Equation 3.45	$u = \theta_{\text{base}}(t)$

Table 3.1: Model variations, dynamics, and controls.

the system can be described as

$$\Omega_{\text{tip}} = V_1 v + V_2 \left(C(t)\mathbf{q} + D(t)u \right),$$

$$\dot{\mathbf{q}} = A(t)\mathbf{q} + B(t)u.$$

(3.47)

To compare controllers built on our general torsional model with previous methods, we choose local coordinates for the tip of the needle, namely Z-Y-X Euler angles (α, β, γ) for orientation and (x, y, z) for position as in Kallem and Cowan [25]. Following Kallem and Cowan further, we define the control task to be controlling the tip of the needle to an arbitrary plane in the tissue. With this control objective in mind, we can choose the local coordinates such that these local coordinates, $\mathbf{s}^T = \begin{bmatrix} x & y & z & \alpha & \beta & \gamma \end{bmatrix}$, are relative to the plane. That is, (y, z) are the position of the needle tip projected to the plane, x is the orthogonal distance from the plane, and α is the rotation of the needle about an axis orthogonal to the plane. The remaining parameters, β and γ, represent the pitch away from the plane and the rotation about the tip of the needle, respectively. The velocities in local coordinates can be related to the velocities in the body-fixed frame via the appropriate Jacobian,

$$\dot{\mathbf{s}} = J^{-1}(\mathbf{s})\Omega_{\text{tip}}.$$

(3.48)

Coupled with the torsional dynamics, the system can be represented as

$$\begin{bmatrix} \dot{\mathbf{s}} \\ \dot{\mathbf{q}} \end{bmatrix} = \begin{bmatrix} J^{-1}(s)V_1 v + V_2 \left(C(t)\mathbf{q} + D(t)u \right) \\ A(t)\mathbf{q} + B(t)u \end{bmatrix}. \tag{3.49}$$

For the task of controlling to a plane, Kallem and Cowan showed that (3.48) can be further reduced by "throwing away" the states (y, z, α), since they do not couple into the states (x, β, γ), and that $(x, \beta, \gamma) = (0, 0, 0)$ corresponds to the needle tip traveling in the desired plane [25]. Thus, we augment these three states with the torsional states, i.e. $\mathbf{r} = \begin{bmatrix} x & \beta & \gamma & \mathbf{q}^T \end{bmatrix}^T$. In these coordinates, the full needle model with reduced state and torsional dynamics included is

$$\dot{\mathbf{r}} = \begin{bmatrix} v \sin(r_2) \\ \kappa v \sin(r_3) \\ -v\kappa \cos(r_3) \tan(r_2) + C(t)\mathbf{r}_{4\cdots n} + D(t)u \\ A(t)\mathbf{r}_{4\cdots n} + B(t)u \end{bmatrix} \tag{3.50}$$

$$=: f(\mathbf{r}, u, t).$$

Here we have a nonlinear and time-varying system for which we investigate common control practices for dealing with these types of systems. In the following section, we devise a control strategy with the assumption that the orthogonal distance of the needle tip from the plane is our only measurement. In this generic formulation of the complete needle dynamics—kinematic states and torsional states—keep in mind that the matrices $A(t)$, $B(t)$, $C(t)$, $D(t)$, and control input u are specific to the model

chosen to represent the system.

3.3 Control with Time-Varying Torsional Dynamics

Kallem and Cowan used feedback linearization to generate a system for which LQR/LQG control was implemented. Using the model in (3.50), feedback linearization of the complete system is not possible due to the manner in which the control input, u, enters into the system. Any attempt to feedback linearize the kinematic states necessarily introduces a nonlinearity into the torsional states.

The approach we take here is to (1) linearize the system about the origin, (2) define a feedforward control to decouple the kinematic state from the torsional states, and (3) compute the infinite horizon LQR gain to optimally control the decoupled kinematic states to the plane. A key component in this control strategy is to show that the final control input ensures that the torsional state remain bounded for the duration of our insertion.

The linearization of the system representation given in (3.50), which is valid for

any of the system models, about the origin is

$$\dot{\mathbf{r}} = \begin{bmatrix} 0 & v & 0 & 0 \\ 0 & 0 & \kappa v & 0 \\ 0 & -\kappa v & 0 & C(t) \\ 0 & 0 & 0 & A(t) \end{bmatrix} \mathbf{r} + \begin{bmatrix} 0 \\ 0 \\ D(t) \\ B(t) \end{bmatrix} u. \tag{3.51}$$

Let the control input be defined as

$$u = \frac{1}{D(t)} \left(-C(t)\mathbf{r}_{4\cdots n} + u_2(t) \right). \tag{3.52}$$

The first term decouples the kinematic and torsional states. This results in

$$\dot{\mathbf{r}} = \begin{bmatrix} 0 & v & 0 & 0 \\ 0 & 0 & \kappa v & 0 \\ 0 & -\kappa v & 0 & 0 \\ 0 & 0 & 0 & A(t) - \frac{1}{D(t)}B(t)C(t) \end{bmatrix} \mathbf{r} + \begin{bmatrix} 0 \\ 0 \\ 1 \\ \frac{1}{D(t)}B(t) \end{bmatrix} u_2(t). \tag{3.53}$$

The first three states of the decoupled system are controllable and we implement a controller of the form

$$u_2(t) = \begin{bmatrix} k_1 & k_2 & k_3 & 0 & \cdots & 0 \end{bmatrix} \mathbf{r}, \tag{3.54}$$

where the gain is from the infinite horizon LQR solution to minimize the cost function

$$J = \int_{t_0}^{\infty} \mathbf{r}_{1\dots3}^T(\tau)Q\mathbf{r}_{1\dots3}(\tau) + Ru_2^2(\tau)d\tau. \tag{3.55}$$

As in the previous section, where we provided a generic formulation of the complete needle dynamics given a model choice, this control scheme is also presented generically and an implementer should keep in mind that the matrices $A(t)$, $B(t)$, $C(t)$, $D(t)$, and control input u are specific to the model chosen to represent the system. However, the same decoupling and subsequent LQR control is valid for any of the model variations.

Heretofore we have assumed full state feedback, but in practice we are only able to measure a scalar output, the distance from the desired plane,

$$y = \begin{bmatrix} 1 & 0 & \cdots & 0 \end{bmatrix} \mathbf{r}$$
$$= r_1. \tag{3.56}$$

Fortunately, a straight forward calculation can be used to verify observability of the system analytically by reconstructing the state from the output and its first $n-1$ derivatives. So, in our simulations and experiments we use a Kalman filter to estimate the states of the linearized system (3.51) with the measurement model given in (3.56), and apply state feedback on this estimate, as is standard practice.

3.4 Experimental Results

Here we present simulations and experiments to demonstrate that the modeling and control methods described herein provide an improvement over existing control methods which do not compensate for torsional dynamics during insertion. In lieu of a systematic approach for model reduction (e.g. based on the Hankel singular values) for this LTV system, we compare control efficacy based on models of different orders in an extensive set of simulations. We use Model C for all simulations and experiments presented here due to the robot construction only allows control at the base of the needle and we are inserting into a single homogeneous piece of tissue.

Simulations are divided into two categories: 1) deterministic system with full state access and 2) system with process and measurement noise with measurement (3.56) and state estimate via a Kalman filter. The pilot experiments with the needle insertion robot are also conducted with the model assuming process and measurement noise as state estimate via a Kalman filter. The measurement model (3.56), the orthogonal distance from the plane to which we are working to converge, is obtained through stereo triangulation of the needle tip from stereo cameras and semi-transparent plastisol as a tissue surrogate.

In all simulations, we use a 25th order torsional truncation as the "real" system. That is the dynamical equations that are integrated to represent the true evolution of system state is based on the torsional dynamics Model C that has 25 states. In reality, the system is infinite dimensional and not amenable to concrete computations in its

Parameter	Value
Density (ρ)	$6.45 \times 10^3 \ \frac{\text{kg}}{\text{m}^3}$
Polar moment of inertia (J)	$2.3572 \times 10^{-14} \ \text{m}^4$
Shear modulus (G)	2.72×10^{10} Pascals
Viscous drag (β)	$2.23 \times 10^{-2} \ \text{N} \cdot \text{m} \cdot \text{s}$
Radius of curvature $(1/\kappa)$	0.122 m

Table 3.2:   Parameters used in simulations shown in Figure 3.6.

complete representation. The choice of 25 states was based on the amount of time required to generate the model via Mathematica and integrate the system dynamics for the simulations. In both simulations and experiments we show results associated with representing the torsional dynamics with 1, 5, and 25 truncated states and show that, for the parameters of our setup, five modes are sufficient. Table 3.2 lists parameters used for all simulations, derived by dimensionally scaling the parameters given by Reed et al. [43] to match the needle geometry of Kallem and Cowan [25]. Here, the viscous drag is assumed to scale linearly as a function of surface area and the polar moment of inertia scales as a function of the needle radius.

3.4.1   Numerical simulations suggest that higher order models can improve robustness to noise

We conducted two series of simulations to identify the effect of model order on control of the needle tip to the plane: 1) deterministic control with full state access and 2) control of a noisy system with reduced measurements. The deterministic simulations allow us to identify the best possible performance for our control method.

The noisy system and reduced measurements are more indicative of the conditions experienced during real experimentation. Neither simulation is an exact representation as we simulate the "real" system with a 25-state representation of the torsional dynamics. A higher order model could have been generated at the cost of prohibitively long Galerkin projections in Mathematica, and since we found that the fifth-order modal model almost exactly reproduces the twenty-fifth-order model, we are reasonably confident that 25 modes is more than sufficient to capture the dynamics for simulations.

Figure 3.6 shows the results of the simulations for a system with parameters given in Table 3.2 and 15 cm of insertion at 1 cm/sec. The results of the deterministic simulation with full state access, shown in Figure 3.6(A), show the best possible rate of convergence given the decoupling feedback with LQR control for convergence to the plane. The results of the simulations with process and measurement noise, with a Kalman filter for state estimation, are shown in Figure 3.6(B-D) for the 25-, 5-, and 1-state models, respectively. Here the state estimate was used for feedback control. These results indicate that all controllers (based on different order modal models) exhibit similar rise times, but the overshoot and final settling time improves with increased model order. In all cases, we conducted one thousand trials for each of the simulated systems. The center line of (A-D) represents the mean trajectory over the 1000 trials. For (B-D), where process and measurement noise affected the insertion trajectory, the shaded region represents the standard deviation of the ensemble over

the 1000 trials.

3.4.2 Physical experiments suggest that one modal state is sufficient to enhance control

We conducted preliminary experiments with our needle insertion robot and artificial tissue (plastisol). The experimental setup consists of an industrial PC running a modified Ubuntu installation with RTAI realtime extensions (www.linuxcnc.org), stereo cameras for needle tip triangulation, and our needle insertion robot (the system is similar to that of Kallem and Cowan [25]). For these experiments we performed a single insertion without rotating at the base and fit a circle to the recorded tip measurements to identify the radius of curvature. Values for viscous drag and polar moment of inertias were obtained by dimensionally scaling the reported results in [43] based on our needle diameter of 0.635 mm. The viscous drag is assumed to scale linearly as a function of surface area and the polar moment of inertia scales as a function of the needle radius. The radius of curvature was determined experimentally by performing several insertions without twisting at the base and averaging the radius of curvature of circles fit to the needle trajectories.

Figure 3.7 shows the results of 5 experiments for each model order. These preliminary experiments show very little difference between each of estimator/controller pairs based on the different model orders. We suspect that some of this is due to the model parameters being inaccurate and in future experiments we will characterize
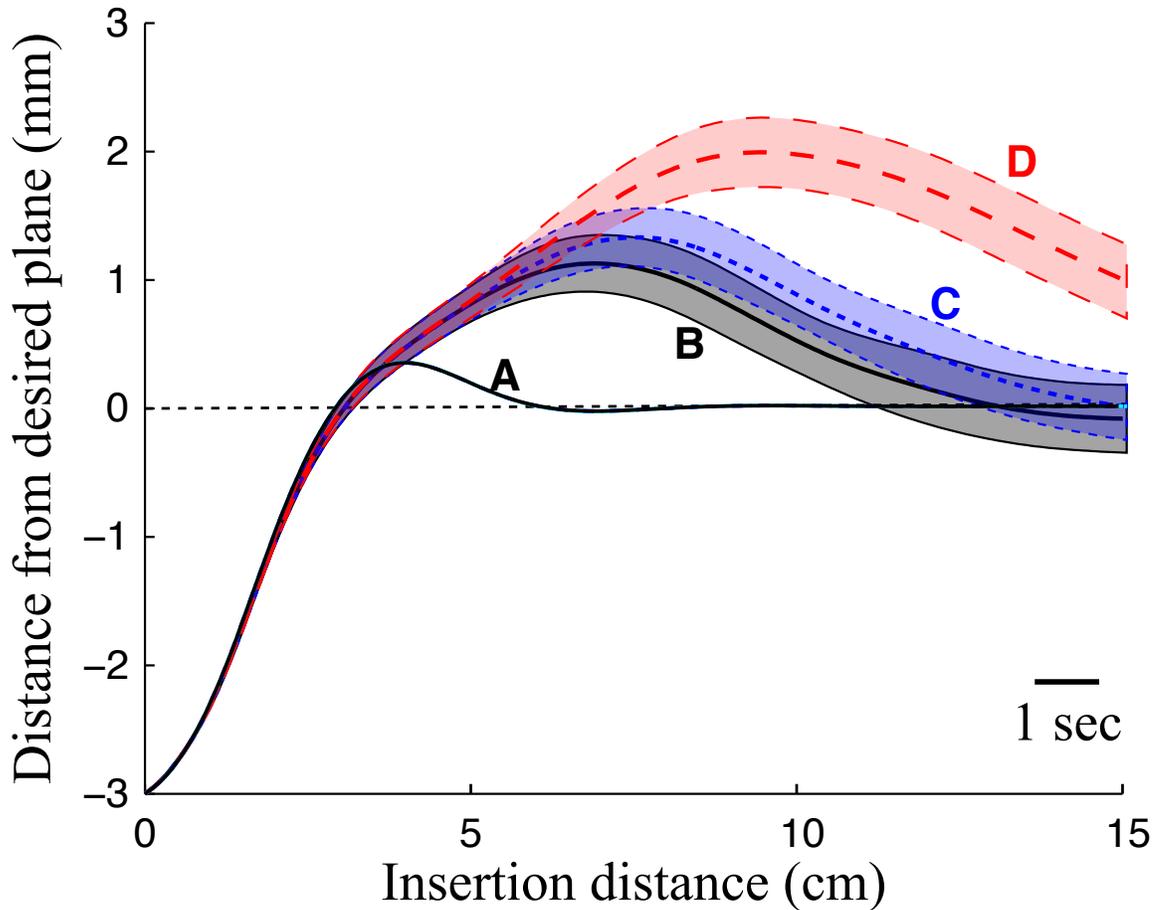
Figure 3.6: Simulation results for 15 cm insertions at $v = 1$ cm/s. All simulations assume a "real" system of 25 modal states, but the feedback control is based on either 1, 5, or 25 modal states. **(A)** Deterministic simulation using a control signal based on 1 modal state and full-state feedback. Note that noiseless, full-state controllers with 5 and 25 modal states were virtually indistinguishable from this trajectory given the parameters of Table 3.2. **(B, C, D)** Estimator-based output feedback control assuming process and sensor noise. The mean trajectory (center line, solid or dashed) and standard deviation (shaded regions) for 1000 trials of each model order are shown: **(B)** The 25 modal state model, **(C)** the 5 modal state model, and **(D)** the 1 modal state model. Here we see that more torsional states can improve performance when using estimator-based output feedback.

the model parameters explicitly for each needle/tissue pairing, rather than relying on previous results.

3.5   Conclusions

This chapter presented a new model for torsional dynamics, that takes into account time-varying boundary conditions. The primary conclusion from our experimental results is that the incorporation of these time-varying dynamics into a closed-loop control scheme significantly improves performance over the purely kinematic control method used previously. Specifically, the experimental trials reported in Kallem and Cowan [25], which did not incorporate torsional dynamics into the control algorithm, required an insertion distance of about 8 cm to recover from a 3 mm initial error from the desired plane. Here we show experimental convergence to the plane in approximately 2.5–3 cm of insertion despite a larger initial error from the plane of 6 mm. Future experiments should evaluate both algorithms using the exact same tissue and needle for a more equitable comparison.

Interestingly, the physical experiments showed a faster than expected convergence for the model with a low number of torsional states. The model order did not seem to have a great impact on the rate of convergence for the physical experiments. This may indicate that our noise parameters in the simulations were significantly greater than those of the real system. It could also be the effect of using a pre-bent needle and the associated unmodeled tip motion when rotating the needle at the base. To
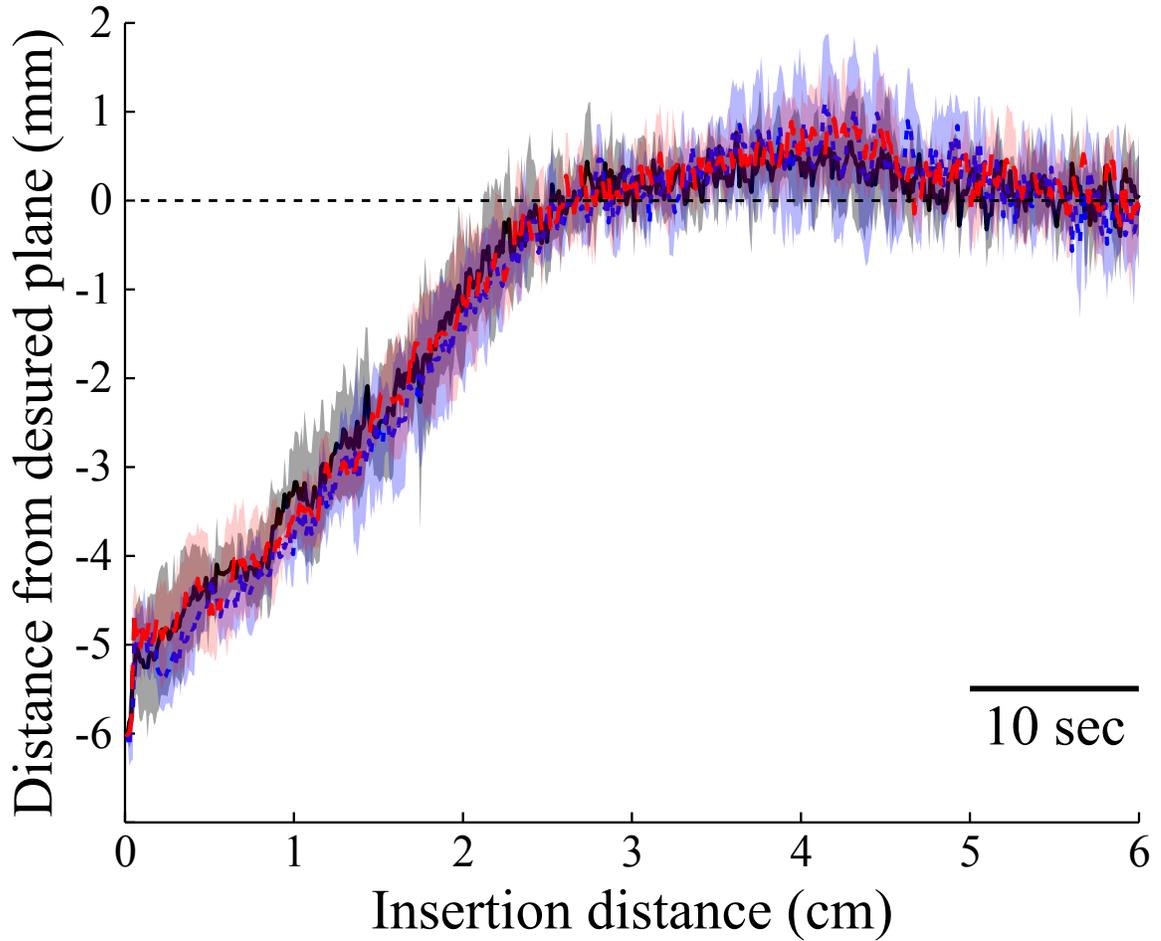
Figure 3.7: Physical experiments for 6 cm insertions at $v = 1$ mm/s. These results show little difference between different model orders, but categorical improvement over previously reported experimental control results [25]. The mean trajectory and standard deviation for 5 trials of each model order are shown, with an initial error of 6 mm from the desired plane: 1 modal state (red), 5 modal states (blue), and 25 modal states (black). Note scale differences when comparing with Figure 3.6.

examine this more carefully requires a careful system identification of noise and system

parameters, which will be the subject of future studies.

Chapter 4

An Almost Global Estimator on $SO(3)$

4.1   Introduction

Many developments in control theory over the past 50 years have been driven by the desire for better attitude determination and control. Much of this work focuses on satellite attitude regulation, but estimation and control on the rotation group applies to a wide range of problems. Our particular treatment of the attitude estimation problem is motivated by the task of controlling of tip-steerable needles [42, 50]. The heart of our problem lies in estimating all three degrees of freedom of rotation given only a two degree-of-freedom measurement in the form of a unit vector—in our case, this unit vector corresponds to one of the columns of the rotation matrix. The goal is

to determine the entire rotation matrix asymptotically, given that measurement plus knowledge of the control input.

This application drives the need for an estimator on SO(3) from measurement restricted to S^2, a result that could apply to any number of other fields involving attitude estimation for rotating rigid bodies. One example is attitude estimation in an underwater vehicle based on a gravity sensor or compass heading. In this chapter, we demonstrate an essentially global estimator for this problem; convergence only fails for initial estimates that are π radians away from the actual state—a set of measure zero [2]. Here, for the three-dimensional space SO(3), measure zero implies that the set has zero volume. The proof of convergence is given using (local) exponential coordinates that are valid over the entire domain of attraction. The method extends easily to the measurement of multiple vectors, for which the convergence proof becomes trivial. Our estimator is invariant in the sense that it is described by a matrix differential equation with the property that when the initial condition is on the manifold described by the Lie group SO(3), exactly integrating the matrix differential equation will result in the estimate remaining in SO(3) for all time.

4.1.1 Related work

Since the advent of the Kalman filter—the optimal *linear* filter—five decades ago, the standard approach for nonlinear systems has been to wrangle the system into a form amenable to applications of the Kalman filter, through coordinatization and

linearization. As most problems are ultimately inherently nonlinear, this technique has been the practical, albeit suboptimal, workhorse of the state estimation systems for spacecraft, aircraft, submarines, and many other noisy nonlinear systems. However, the method is fraught with pitfalls of divergence due to initial conditions and singularities in representation and statistics [14, 30].

In the search for an optimal invariant filter with robustness to initial error, it appears the field is taking the opposite route to Kalman and Luenberger, where the stochastic and deterministic cases were treated in that order in 1961 and 1964, respectively. Recent work by Bonnabel, Mahony, and others has begun to develop a principled framework for defining convergent, invariant observers [5, 6, 28, 31]; much of this recent development takes advantage of the Lie group structure of SO(3).

Markley [34] attempted to develop an invariant filter, but the tools to solve the Fokker-Planck equations exactly were not available and many simplifying assumptions were made, rendering the solution suboptimal in a similar sense to an extended Kalman filter. The natural next step is to develop convergent invariant filters evolving from these invariant observers, as Kalman filters are to Luenberger observers. Recent work in stochastic processes on matrix Lie groups by Park and Chirikjian [10, 41] may provide the tools necessary to analytically solve (or at least approximate) the Fokker-Planck equations, where it was previously not possible. More recently, work by Bonnabel [7] implements an invariant extended Kalman filter (IEKF) using their invariant observer structure to propagate state and using a linearization of the system

for propagating statistics, which is optimal in the same sense that the EKF is approximately optimal for non-invariant observer representations of non-linear systems.

Recently Kinsey and Whitcomb developed invariant adaptive identifier methods for systems in which the (unknown) attitude was fixed and the inputs and the outputs of the system were known [27]. The work presented here is similar in the choice of output error, except we allow the attitude of the system to be time varying. Another recent application was invariant estimation of the homography between stereo cameras [32]. One can imagine that the techniques could also be applied to the many applications in physics described by finite dimensional matrix Lie groups [21].

For our specific application of needle steering, previous work has been done to develop controller and estimator pairs in a reduced set of local coordinates [23–25]. These methods were used for both state estimation and control to a surface defined as part of the state reduction.

The key contribution of our estimator is to provide a nonlinear output injection term into the tangent space of the estimator configuration space—a copy of SO(3)— and to cast the resulting error dynamics as a nonautonomous matrix differential equation. Given this differential equation, we provide an associated proof of almost global convergence of the estimator error to the identity matrix. The nonlinear output injection is a function of the measurement of a single vector between the center of rotation and a point on the rotating body. To the best of our knowledge, the requirement of only one measurement vector is a less restrictive measurement model than all other

invariant estimator work to date. This includes the most recent and complete work in this field about which we are aware [28] which requires multiple measurements or full state access. Of course, at present our method does not constitute a filter, much less an optimal filter; the previous discussion of attitude filtering defines our eventual goal for both needle steering and attitude determination in general.

4.1.2 Chapter Organization

Section 4.2 describes the motivating example of needle steering and the generic plant and measurement model for any rotating rigid body; it also provides a general definition of invariant estimation on the group of rigid body rotations. In Section 4.3, we prove that the system is observable for our plant and measurement model. Section 4.4 defines our contribution of a nonlinear output injection term for the invariant estimator and provides the associated analysis of almost-global asymptotic stability. In Section 4.5 we present several illustrative simulations of the method, for both needle steering and an arbitrary rotating rigid body. We conclude with a few observations and proposed directions for further research.

4.2 Motivation and Plant Model

The principal application that motivates the present study is the problem of estimating the orientation of a flexible, tip-steerable needle [42,50], as depicted in Figure

4.1(A). As these needles are inserted into tissue, the tip asymmetry causes the needle to deflect and follow a circular arc. Rotation of the needle shaft outside the patient causes the needle to act as a flexible drive shaft, reorienting the asymmetric tip before subsequent insertions.

Needle tip motion can be described as a left-invariant kinematic vector field on SE(3) [50]. For planning and control, one would ideally have an estimate of the position and orientation of the body-fixed frame at the tip of the needle. Unfortunately, current medical imaging modalities such as bi-plane fluoroscopy can only be used to extract five degrees of freedom of the needle: the position in $\mathbb{R}^3$ of the needle tip and the vector direction of the needle in S^2, but the tip orientation about the needle shaft cannot presently be resolved. So, for the present exposition, we assume that we can measure the vector tangent to the needle shaft at the tip (namely, aligned with the x-axis in Figure 4.1(A)) either through external imaging or a magnetic tracking device.

4.2.1 Motivation: Needle Steering

Because the needle tip position can be directly measured, in this work we neglect the positional estimation problem, and focus our efforts on the more challenging attitude estimation problem. The orientation dynamics of a kinematic model of tip-steerable needle motion called the "unicycle model", describe by Webster et al. [50]

and Park et al. [39], can be expressed as follows:

$$(R^{-1}\dot{R})^\vee = u(t) = \begin{bmatrix} \omega(t) \\ 0 \\ -\kappa v(t) \end{bmatrix},$$

$$y = Re_1$$

(4.1)

where κ is the instantaneous curvature about the z-axis of the needle path during insertion, ω is the needle shaft rotational velocity, and v is the needle insertion speed. Here, y represents the measurement of the orientation of the x axis. The operators $\widehat{}: \mathbb{R}^3 \to \mathfrak{so}(3)$ and $^\vee: \mathfrak{so}(3) \to \mathbb{R}^3$ denote the usual isomorphism between $\mathbb{R}^3$ and $\mathfrak{so}(3)$, the Lie algebra of SO(3).

The practical question addressed in this chapter is how to estimate $R(t) \in \mathrm{SO}(3)$ asymptotically based on the measurement $y(t) \in \mathrm{S}^2$.

4.2.2 Plant Model and Measurement Model

As a slight generalization of the needle steering orientation estimation problem, we consider a kinematic rotating rigid body in which the angular velocity with respect to the body fixed frame is known; see Figure 4.1(B). As depicted, we also assume that we can measure a single point a unit distance from the center of rotation of the rigid body. For sake of notational simplicity and without loss of generality, we assume that this point is aligned with the first axis of the rigid body.
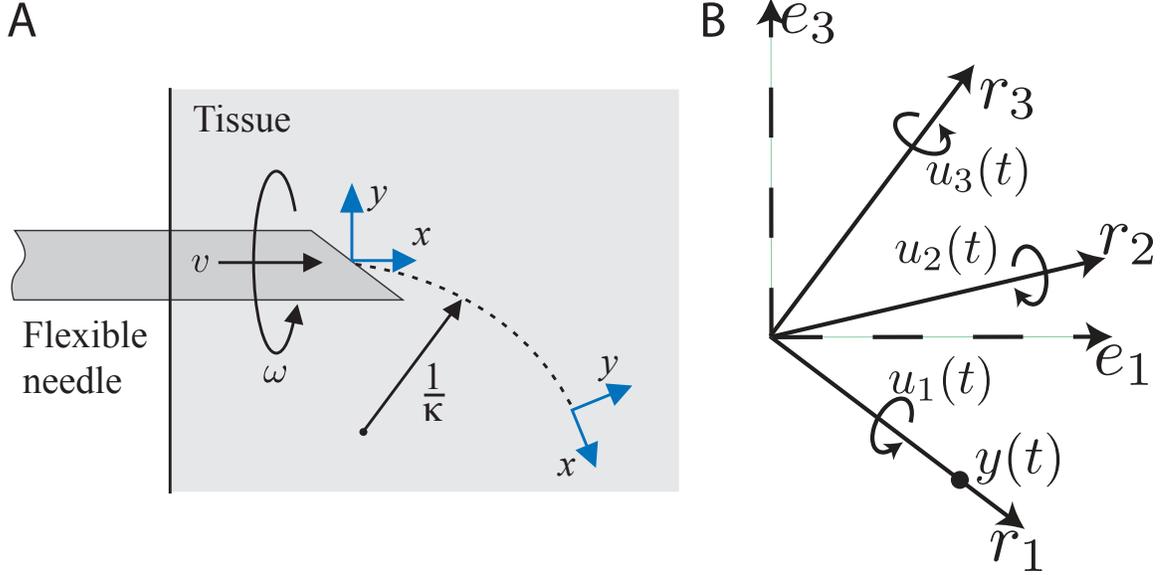
Figure 4.1: Kinematic models for a rotating rigid body. (**A**) Kinematic model used to represent the insertion of tip-steerable flexible needles [50]. As the needle is inserted at velocity v, a bevel or other tip asymmetry causes a lateral force that deflects the needle along a curved path of radius $1/\kappa$. Rotations about the base of angular velocity ω reorient the bevel tip (Modified with permission from [41]). (**B**) General rotating rigid body model (that includes the needle kinematic model). The body frame velocities, $u_i \in \mathbb{R}$, about each rotation axis $r_i \in \mathbb{R}^3$, $i = 1, 2, 3$, are known. The unit vectors e_i, $i = 1, 2, 3$, represent the world frame. The measurement (or output model) is a single vector, $y(t)$, defined by a point on the rotating rigid body with respect to the center of rotation; as depicted, we assume (without loss of generality) that $y(t) = Re_1 = r_1$.

Consider the left invariant kinematic system described using the Lie group $SO(3)$ and its corresponding Lie algebra $\mathfrak{so}(3)$,

$$R^T \dot{R} = \hat{u}, \tag{4.2}$$

with output map

$$y = Re_1. \tag{4.3}$$

We assume that we know the body frame velocities of the rigid body, u.

4.2.3 Problem Statement

We wish to define an invariant estimator for $R(t) \in \mathrm{SO}(3)$ for the system defined by (4.2)–(4.3). The estimator should be invariant in the sense that the estimate $\widetilde{R}$ should evolve on the manifold SO(3). We seek an estimator that converges asymptotically to the true value, $R(t)$, as $t \to \infty$ from essentially any initial condition in SO(3). As will be seen, this will require us to put some constraints on the control inputs, $u(t)$.

Our estimator structure is defined on SO(3) by

$$\tilde{R}^T \dot{\tilde{R}} = \hat{u} + g(y, \tilde{y}), \tag{4.4}$$

where the estimator output is

$$\tilde{y} = \tilde{R}e_1, \tag{4.5}$$

and $g(y, \tilde{y}) \in \mathfrak{so}(3)$.

4.3 Observability of a Kinematic Rigid Body Based on a Single Vector Measurement

Before presenting our observer formulation, we examine the observability of the dynamics given by (4.2)–(4.3).

4.3.1 Observability

A first step to solving the estimation problem is to ascertain whether the system is observable with the measurement given in (4.3) of a single point on the rigid body. One notion of observability is whether the state of the system can be determined from the output of the system and its $n-1$ derivatives [20]. Our approach follows Kallem et al. [24] for slightly different plant and output models.

Lemma 4.3.1. *The system described in* (4.2) *and* (4.3) *is observable at time t pro-vided the velocity control input* $u(t) = \begin{bmatrix} u_1 \\ u_2 \\ u_3 \end{bmatrix} \notin span(e_1)$ *is known.*

Proof. The output and its first time derivative are

$$y = Re_1 = \mathbf{r}_1 \tag{4.6}$$

and

$$\dot{y} = \dot{R}e_1 = RR^T\dot{R}e_1 = R\hat{u}e_1 = R\begin{bmatrix} 0 \\ u_3 \\ -u_2 \end{bmatrix}. \tag{4.7}$$

Manipulating these expressions, one can show that

$$\mathbf{r}_2 = \underbrace{\frac{u_2}{u_2^2 + u_3^2}}_{\alpha}(y \times \dot{y}) + \underbrace{\frac{u_3}{u_2^2 + u_3^2}}_{\beta}\dot{y}, \tag{4.8}$$

77

and thus

$$\mathbf{r}_3 = \mathbf{r}_1 \times \mathbf{r}_2 = \alpha \left[y \times (y \times \dot{y}) \right] + \beta (y \times \dot{y}). \tag{4.9}$$

We see that if the restriction placed on the control input is violated, then the computation of (4.8) becomes ill defined. $\qquad\qquad\qquad\square$

Note that observability of (4.2)–(4.3) requires that the control input not correspond to a pure rotation about the output vector, i.e. $u \notin \mathrm{span}(e_1)$. This implies u_2 and u_3 cannot both be zero—such a rotation renders $y = \mathrm{const.}$, making it impossible to infer the final degree of freedom.

4.4 Invariant Observer for Attitude Estimation

In this section, we develop an estimator for the attitude of the rigid body that is almost globally convergent, with the exception of a set of initial conditions of measure zero. Many techniques for attitude estimation employ embeddings or coordinatizations (in the context of needle steering, see [24]) of the rotation matrix describing the attitude of the rigid body. Our estimator consists of a matrix differential equation evolving on the manifold SO(3), such that the estimator state remains on the manifold for all time.

Given the representation of the kinematic rotating rigid body (4.2)-(4.3), we pro-

pose the following as the estimator correction term for the estimator (4.4)-(4.5):

$$g(y, \tilde{y}) = k\tilde{R}^T \widehat{(y \times \tilde{y})}\tilde{R}, \tag{4.10}$$

where k is the observer gain. Note that $g(y, \tilde{y})$ lies in $\mathfrak{so}(3)$, ensuring that the estimator evolves on SO(3).

In the absence of a control input, the output injection term (4.10) would cause a rotation of the estimate about an axis mutually orthogonal to both the first column of the estimator, $\tilde{r}_1$, and that of the rigid body, r_1, thereby aligning these two columns asymptotically. Thus the estimator would remain in error by some rotation about e_1, i.e. $\tilde{R} = \exp\{\alpha\hat{e}_1\}R$. Fortunately, when this is the case, "most" inputs to the system drive $\tilde{r}_1$ and r_1 apart, which is at the heart of our invariance-like stability analysis, as shown below.

4.4.1 Stability Analysis

We define the error between the kinematic system and the observer as

$$E = R^T \tilde{R}. \tag{4.11}$$

For a convergent estimator, this error will approach the identity matrix as time approaches infinity. By direct computation,

$$E^T \dot{E} = \hat{u} - E^T \hat{u} E + k \tilde{R}^T \left(\widehat{y \times \tilde{y}} \right) \tilde{R}. \tag{4.12}$$

Since

$$y \times \tilde{y} = (Re_1) \times (\tilde{R}e_1) = R\hat{e}_1 Ee_1, \tag{4.13}$$

the body-frame error velocities are given by

$$\Omega_E = (E^T \dot{E})^\vee = u - E^T u - k\hat{e}_1 E^T e_1. \tag{4.14}$$

Before proceeding to develop a candidate Lyapunov function, we point out an important property of the velocities of error system (4.14): they have no explicit dependence on the actual state of the system, $(R(t), \widetilde{R})$, but rather only depend on the error between them. While this is a standard result for the LTI Luenberger observer, this is not generally true of nonlinear systems; for other choices of nonlinear output injection than (4.10), the body frame error will typically depend on both R and $\widetilde{R}$.

Also particularly interesting is the fact that the body-frame error velocities are not left invariant, nor are the spatial frame error velocities right invariant. Often in the rotation of rigid bodies, velocities are written in the body frame form or spatial frame

form because the dynamics are either left invariant or right invariant. This allows the analysis of motion to be independent of the state of the system. That is, *if* the body fixed frame velocities are left invariant, then the actual rotation of the rigid body has no effect on the vector field representing the body fixed frame in the Lie algebra at the identity configuration. In our case, the lack of an obvious left or right invariant representation forces us to analyze a system where initial conditions and system state matter. However, the lack of an obvious left or right invariant representation of velocities does not preclude the possibility of a virtual frame attached to the rigid body, most likely time varying, that would result in a left or right invariant representation of the system. We have not yet found such a representation and proceed to show asymptotic stability of the error system without such a representation.

Now, we represent the error system in terms of exponential coordinates,

$$E = \exp(\hat{x}), \tag{4.15}$$

which serve as local coordinates for stability analysis of estimator error. Note that our choice of coordinates cover all of SO(3), excluding a thin set of rotations, namely rotations about any axis of π radians.

The Jacobian between exponential coordinates and body-frame velocities [38] al-

lows us to recast (4.14) in terms of exponential coordinates via $\dot{x} = J_R^{-1}(x)\Omega_E$, namely:

$$\dot{x} = J_R^{-1}(x)\left[u(t) - \exp(\hat{x}^T)u(t) - k\hat{e}_1\exp(\hat{x}^T)e_1\right]$$
$$= f(x,t).$$

(4.16)

Equation (4.16) represents the flows of the error system in terms of a typical nonlinear, nonautonomous differential equation.

Consider the following candidate Lyapunov function on the local coordinates of the error system,

$$V = \frac{1}{2}x^T x,$$

(4.17)

with time derivative

$$\dot{V} = x^T\dot{x}$$
$$= x^T J_R^{-1}(x)\Omega_E$$
$$= x^T\Omega_E$$
$$= x^T\left(\underbrace{u - E^T u}_{A} + k\underbrace{\widehat{E^T e_1}e_1}_{B}\right).$$

(4.18)

The penultimate step of (4.18) is due to the fact that x is a left eigenvector of $J_R^{-1}(x)$ associated with a unity eigenvalue. We are now left to show that the time derivative of the Lyapunov function implies asymptotic stability. The following computations show that $\dot{V}$ is negative semi-definite for the chosen Lyapunov function. This is accomplished by expanding the error state, E, in (4.18) using the Rodrigues formulation

for exponential coordinates given in (4.15) and writing x in axis and angle form:

$$\phi = \|x\|, \quad \hat{q} = \frac{\hat{x}}{\|x\|}.$$ (4.19)

Then, A from (4.18) can be simplified as

$$
\begin{aligned}
A &= u - \left(I - \hat{q}\sin(\phi) + \hat{q}^2(1 - \cos(\phi))\right)u \\
&= u - u + \sin(\phi)\hat{q}u - (1 - \cos(\phi))\hat{q}^2 u \\
&= \sin(\phi)\hat{q}u - (1 - \cos(\phi))\hat{q}^2 u \\
&= -\sin(\phi)\hat{u}q - (1 - \cos(\phi))\hat{q}^2 u.
\end{aligned}
$$ (4.20)

A similar computation yields B from (4.18):

$$B = -\sin(\phi)(e_1 e_1^T - I)q - (1 - \cos(\phi))\left[\hat{e}_1 q q^T e_1\right].$$ (4.21)

Thus, the body frame error velocity (4.14) is

$$
\begin{aligned}
\Omega_E &= A + kB \\
&= -\sin(\phi)\hat{u}q - (1 - \cos(\phi))\hat{q}^2 u + \\
&\quad k\left(-\sin(\phi)(e_1 e_1^T - I)q - (1 - \cos(\phi))\left[\hat{e}_1 q q^T e_1\right]\right).
\end{aligned}
$$ (4.22)

Using (4.20) and (4.21),

$$
\begin{aligned}
\dot{V} =&\, x^T \left(A + kB \right) \\
=&\, \phi q^T (- \sin(\phi) \hat{u} q - (1 - \cos(\phi)) \hat{q}^2 u \\
&\, - k \sin(\phi)(e_1 e_1^T - I) q \\
&\, - k(1 - \cos(\phi)) \left[\hat{e}_1 q q^T e_1 \right]) \\
=& - \phi \sin(\phi) q^T \hat{u} q^{\;0} - \phi(1 - \cos(\phi)) q^T \hat{q}^2 u^{\;0} \\
&\, - k\phi \sin(\phi) q^T (e_1 e_1^T - I) q \\
&\, - k\phi(1 - \cos(\phi)) q^T \hat{e}_1 q q^T e_1^{\;0} \\
=& - k\phi \sin(\phi) q^T (e_1 e_1^T - I) q \\
=&\, x^T \underbrace{\left(-k \operatorname{sinc}(\phi) \hat{e}_1^2 \right)}_{M(\phi)} x \\
\leq&\, x^T \underbrace{\left(-k \operatorname{sinc}(\phi(t_0)) \hat{e}_1^2 \right)}_{M(\phi(t_0))} x \\
=&\, V^*(x) \leq 0 \quad (\forall k < 0).
\end{aligned}
\tag{4.23}
$$

Note that $\operatorname{sinc}(\phi) > 0$ on $\phi \in [0, \pi)$ and $\hat{e}_1^2$ is negative semidefinite; thus for $k < 0$ then $\dot{V} \leq 0$. We see that the time derivative of the chosen Lyapunov function is only negative semi-definite in the parameterized error coordinates and Lyapunov analysis only guarantees asymptotic convergence to the set $\{x : V^*(x) = 0\} = \{x : x = \alpha e_1, \alpha \neq 0\}$, or, equivalently, the set $\{x : \dot{V} = 0\}$.

To show asymptotic convergence to $x = 0$, we now must consider whether the

control input renders the system, in global and local coordinates given in (4.12) and (4.16) respectively, autonomous or nonautonomous. In the case of a control input that is constant or a function of state, the system is autonomous and we can proceed with a straightforward proof using LaSalle's invariance principle and the Barbashin-Krasovskii theorem [3,26]. For an arbitrary control input, an explicit function of time, we resort to one of the techniques called "invariance-like" methods by Khalil [26]. In particular, we use the theorem first presented by Matrosov [48] and extended to non-scalar auxiliary functions by Rouche [44]. We refer readers to the translated Matrosov paper and the Rouche paper for proofs of the original theorems.

Aside 1: Arbitrary measurement—$y = R(t)v^*$

We earlier discussed the choice of using e_1 in the output map to clarify the presentation. Here, we point out that had we chosen a different vector in the output map, say $y(t) = R(t)v^*$, then the matrix $M(\phi)$ in (4.23) would still be a rank 2 matrix with v^* lying in the null space, and the points to which Lyapunov analysis guarantees asymptotic convergence are the scalar multiples of v^*.

Aside 2: Multiple linearly independent measurements—$y_i = R(t)v_i^*, i \in \{1, \cdots, n\}$

When multiple measurements are available, the output injection term in (4.10) can be written as a sum of the cross products of the outputs,

$$g(y, \tilde{y}) = \sum_{i=1}^{n} k_i \tilde{R}^T (\widehat{y_i \times \tilde{y}_i}) \tilde{R}, \tag{4.24}$$

where each k_i is the observer gain for the respective measurement. The result is the time derivative of the Lyapunov equation:

$$\begin{aligned}
\dot{V} &= \sum_{i=1}^{n} x^T \underbrace{\left(-k_i \mathrm{sinc}(\phi)(\hat{v}_i^*)^2\right)}_{M_i(\phi)} x \\
&= -\mathrm{sinc}(\phi) x^T \left(\sum_{i=1}^{n} k_i (\hat{v}_i^*)^2\right) x.
\end{aligned} \tag{4.25}$$

We then investigate the definiteness of this sum of matrices.

Lemma 4.4.1. *Given two negative semi-definite matrices $M_i, M_j \in \mathbb{R}^{n \times n}$ where $Null(M_i) \neq Null(M_j)$, then $Null(M_i + M_j) = \{\emptyset\}$ and $M_i + M_j$ is negative definite.*

Proof. Given a vector $u \in \mathrm{Null}(M_i)$ and $v \in \mathrm{Null}(M_j)$, because the null spaces have differing spans then u and v are linearly independent. Next, create a basis for the entire n-dimensional space using u, v, and Graham-Schmidt to complete the basis with vectors $\{w_i\}$. Then, any vector $z \in \mathbb{R}^n$ can be written in terms of this basis. The two problem cases are when $z = \alpha u$ or $z = \alpha v$. A matrix M is said to be negative

definite if $\forall z \in \mathbb{R}^n$, $z^T M z < 0$. For any vector written in the new basis,

$$z^T(M_i + M_j)z = (a_1 u + a_2 v + \sum_{i=1}^{n-2} a_{i+2} w_i)^T (M_i + M_j)(a_1 u + a_2 v + \sum_{i=1}^{n-2} a_{i+2} w_i)$$

$$= z^T M_i z + z^T M_j z.$$

Any vector z cannot simultaneously lie in the null space of M_i and M_j, thus $\text{Null}(M_i + M_j) = \{\emptyset\}$. Consequently, $z^T M_i z + z^T M_j z < 0$ by the negative semi-definiteness of M_i and M_j individually. □

Thus for the multiple measurement case, $\dot{V} < 0$ and traditional Lyapunov theory guarantees asymptotic convergence, without resorting to the invariance-like methods used subsequently in the single measurement case. However, when multiple linearly independent measurements are available the rotation matrix can be solved for exactly. The observer formulation, rather than the exact solution, could provide benefits of filtering when utilizing this deterministic observer on a stochastic system.

4.4.1.1 The vector-field on the set $\mathcal{M} = \{x : \dot{V} = 0\}$

From (4.14) note that when $q = e_1$ (i.e. $x = \alpha e_1$) we have

$$\Omega_E = [I - E^T]u, \tag{4.26}$$

where $E = \exp(\phi \hat{e}_1)$. Thus, by direct computation

$$\dot{x} = J_R^{-1}(\phi e_1)\Omega_E = \begin{bmatrix} 0 \\ -\phi u_3 \\ \phi u_2 \end{bmatrix}. \tag{4.27}$$

This shows that the non-invariance of $\mathcal{M}$ depends on the control input $u(t)$. If we assume that $u(t)$ is bounded and piecewise continuous in time, then it is easy to show that $f(x,t)$ is differentiable in space and time and thus locally Lipschitz on $\{x \in \mathbb{R}^3 : \|x\| < \pi\}$. Further, we impose a "persistency" condition on $u(t)$, namely that u_2 and u_3 are not both zero simultaneously when the system state is on the problem set $\mathcal{M}$. Written more formally, let

$$u_2^2(t) + u_3^2(t) > \delta^2 > 0 \text{ for } x \in \mathcal{M}. \tag{4.28}$$

We called this a "persistency" condition, in quotes, because it is much less restrictive than the traditional integral form of persistency of excitation as defined in the adaptive systems literature. For this input, it is easy to see from (4.27) that the vector field is transverse to $\mathcal{M}$ instantaneously when on the problem set. We wish to show the vector field is transverse over some nonzero interval of time and hence there exists a time $t_1 > t$ such that $x(t_1) \notin \mathcal{M}$. The existence of a finite time for which $x(t)$ exits an open region containing the problem set lies at the core of the theorems

of Matrosov and Rouche, which can be viewed as analogues to LaSalle's invariance principle for non-autonomous systems.

4.4.1.2 Main Result

Because the control input, $u(t)$, is not necessarily constant, this system is generally nonautonomous and thus the traditional theorems concerning LaSalle's invariance principle are not valid. This is due to the fact that for general nonautonomous systems, the positive limit sets of solutions to the differential equations are not invariant [26].

However, we have a system in which the Lyapunov function and its time derivative are not explicit functions of time, despite the fact that the system is nonautonomous. This simplifying feature of our problem is a direct result of the choice of nonlinear output injection and the resulting independence of the error system (4.14) from the state, R, of the system (4.2). This feature makes the application of the aforementioned invariance-like method more simple to show convergence. Here we restate the theorem as given by Rouche [44] in the notation of this dissertation, without proof, for reader convenience.

Definition 1 (Non-vanishing-definite vector function)**.** *The vector function* $Y(t, x)$: $\mathbb{R} \times B_\rho \to \mathbb{R}^k$, *where* k *is a positive integer, is* **non-vanishing definite on a set** $\mathcal{M}$ *if, for every pair of positive numbers* υ *and* ε *with* $\upsilon < \varepsilon < \rho$, *there is a positive*

number $\xi(\upsilon, \varepsilon)$ and an open covering $\{\pi_1, \pi_2, \cdots, \pi_m\}$ of the set

$$F = \{x : \upsilon \leq \|x\| \leq \varepsilon, d(x, \mathcal{M}) = 0\}$$

such that for every i, $(1 \leq i \leq m)$, there is a component Y_j of Y with the property that $(t \in \mathbb{R})(x \in \pi_i) \Rightarrow |Y_j(t, x)| > \xi$.

Theorem 4.4.2 (Rouche Theorem 4.4 from [44]: sufficient conditions for uniform asymptotic stability). *Let there exist two functions $V(t, x) : \mathbb{R} \times B_{\rho'} \to \mathbb{R}$ and $W(t, x) : \mathbb{R} \times B_{\rho'} \to \mathbb{R}^k$ (k a positive integer), continuous as well as their time derivative $\dot{V}(t, x)$ and $\dot{W}(t, x)$ computed along the solutions of $\dot{x} = f(t, x)$. If*

(a) for all $x \in B_\rho : \|f(t, x)\| \leq A$, where A is a positive constant;

(b) $V(t, x)$ is positive definite; $V(t, x) \to 0$ uniformly in t when $x \to 0$;

(c) there exists a continuous function $V^*(x) : B_{\rho'} \to \mathbb{R}$ such that $\dot{V}(t, x) \leq V^*(x) \leq 0$; $\dot{V}(t, 0) = 0$; we write $\mathcal{M} = \{x : V^*(x) = 0\}$;

(d) for every $L > 0$, there is a $\chi > 0$ such that

$$d(x, \mathcal{M}) \leq \chi \Rightarrow \|W(t, x)\| < L$$

(e) $\dot{W}(t, x)$ is non-vanishing definite on $\mathcal{M}$;

the, the vanishing solution $x \equiv 0$ of the system $\dot{x} = f(t, x)$ is uniformly asymptotically stable.

Using this theorem, we develop a corollary for our error system kinematics.

Proposition 4.4.3 (Corollary to Theorem 4.4.2). *Consider the nonautonomous system represented in local coordinates as given in* (4.16), *with a Lyapunov function and its negative semidefinite time derivative given by* (4.17) *and* (4.23), *respectively. Then, if the control input $u(t)$ is bounded, continuous, and persistently exciting in the sense of* (4.28), *the origin of the error system, $x = 0$ is asymptotically stable.*

Proof. Let

$$W(t, x) = \hat{e}_1^2 x \tag{4.29}$$

with the open balls B_ρ and $B_{\rho'}$ defined with $\rho' = \pi$, $\rho = \pi - \epsilon$, and $\epsilon > 0$.

(a) For bounded control input $u(t)$ and bounded estimator gain k, the body frame velocity Ω_E is bounded. In addition, the Jacobian $J_R^{-1}(x)$ is nonsingular for all $x \in B_\rho$ such that $\exists A > 0$ where the time derivative of the error coordinates are bounded by A, $\|\dot{x}\| = \|f(t, x)\| < A$;

(b) $V(t, x) = \frac{1}{2}x^T x > 0, V(t, 0) = 0$ by construction;

(c) Let $M(\rho) = -k\text{sinc}(\rho)\hat{e}_1^2$ identified with the semidefinite function $M(\cdot)$ given in (4.18). Then the time derivative of the Lyapunov equation is bounded from above as $\dot{V}(t, x) \leq x^T M(\rho)x = V^*(x) \leq 0$ (where $M(\rho)$ is negative semidefinite,

as shown in (4.23)), $\dot{V}(t,0) = 0$, $\forall t > t_0$, and the set where $\dot{V}(t,x) = 0$ is

$$\mathcal{M} = \{x : x = \alpha e_1\};$$

(d) The distance of the current state from the problem set $\mathcal{M}$ is $d(x,F) = x_2^2 + x_3^2$.

The magnitude of the vector valued auxiliary function $W(t,x)$ is $\|W(t,x)\| = x_2^2 + x_3^2$. So for every $L > 0$, let $\chi = \frac{L}{2}$ such that $d(x,\mathcal{M}) \leq \frac{L}{2} \Rightarrow \|W(t,x)\| < L$;

(e) Recall from (4.19) that $x = \phi q$, where $\|q\| = 1$, and note that on the problem set $\mathcal{M}$ the magnitude of the angle error, ϕ, is given by $\phi^2 = \|x\|^2 = x_1^2$, and $q = \pm e_1$. Thus the time derivative of the auxiliary function $W(t,x)$ is

$$\dot{W}(t,x) = \hat{e}_1^2 \dot{x} = \hat{e}_1^2 J_R^{-1}(\phi q)\Omega_E = \pm \begin{bmatrix} 0 \\ x_1^2 u_3 \\ -x_1^2 u_2 \end{bmatrix}, \tag{4.30}$$

We proceed to show that $\dot{W}(t,x)$ is a non-vanishing-definite vector function as defined above. For every υ and ε, with $\upsilon < \varepsilon < \rho$, we define the set of points in $\mathcal{M}$ with distance from the origin in the region $[\upsilon, \varepsilon]$ as

$$F = \{x : \upsilon \leq \|x\| \leq \varepsilon, d(x,\mathcal{M}) = 0\}$$

$$= \{x \in \mathcal{M} : \upsilon \leq \|x\| \leq \varepsilon\}.$$

We can choose as an open covering for F the two open intervals

$$\pi_1 = \left(\frac{\upsilon}{2}, \frac{\varepsilon + \rho}{2} \right)$$

$$\pi_2 = \left(-\frac{\varepsilon + \rho}{2}, -\frac{\upsilon}{2} \right).$$

So, for any $x \in \pi_i$ then, by inspection from (4.30), $\|\dot{W}\|_1 > \frac{\upsilon}{2} \max(u_2, u_3)$. Letting $\xi(\upsilon, \epsilon) = \frac{\upsilon}{2} \max(u_2, u_3)$ there is a component $\dot{W}_j$ of $\dot{W}$ with the property that $(t \in I)(x \in \pi_i) \Rightarrow |\dot{W}_j(t, x)| > \xi$. Thus, $\dot{W}(t, x)$ is a non-vanishing-definite vector function on F.

Since $\rho = \pi - \epsilon$ with $\epsilon > 0$ arbitrarily small, the domain of attraction excludes, at most, rotations of π. $\square$

Note that for the body angular velocities for the specific problem of needle steering, given in (4.1), that the control input will always satisfy the conditions of the theorem, namely that for insertion velocity non-zero $u_3 = \kappa v > 0$.

As one final note, we address a question that naturally arises about our convergence analysis above. Our local coordinates neglect all initial conditions with errors that are rotations of π radians from the identity. Might some, or perhaps all, initial conditions on this set converge? Certainly not all of them: global convergence of a smooth vector field on SO(3) is impossible. Since we exclude only a set of measure zero from our analysis, we do not find this to be a major practical limitation of our approach, especially since truly global convergence is a topological impossibility.

4.5 Numerical Examples

Before describing our numerical examples, we note that a naïve numerical implementation of the estimator (4.4) would typically accumulate round-off errors causing the solution to drift off of SO(3), and while more sophisticated manifold integration schemes exist, we simply employ a fourth-order Runge-Kutta integrator in $\mathbb{R}^9$ with reprojection onto SO(3) at each time step [4].

Since our motivating problem is steering flexible needles, the following examples demonstrate the estimator for two typical types of needle motion: piecewise planar paths and helical paths. These trajectories are depicted in Figure 4.2. Rather than exhaustive numerical tests, these simulations are merely designed to illustrate the potential effectiveness of the proposed techniques to the problem at hand.

We have observed anecdotally that convergence was closely tied to total rotation caused by the input $u(t)$. With a "good" (hand-tuned) choice in gain, we were typically able to achieve a convergence rate of 80% per $\pi\kappa$ units of insertion distance. Figure 4.3 demonstrates the convergence for two different choices in gain for a piecewise planar needle insertion with 720° of rotational motion. The point where $t = 11$ sec represents the accumulation of 180° of rotational motion by the needle. In these trials, we initialized the estimator state by setting the first column of the estimator rotation matrix to the measurement at t_0 with an initial error about the measurement axis of 90°. The key aspect of the estimator gain selection is in choosing the tradeoff between the magnitude of the control input, $u(t)$, which tends to
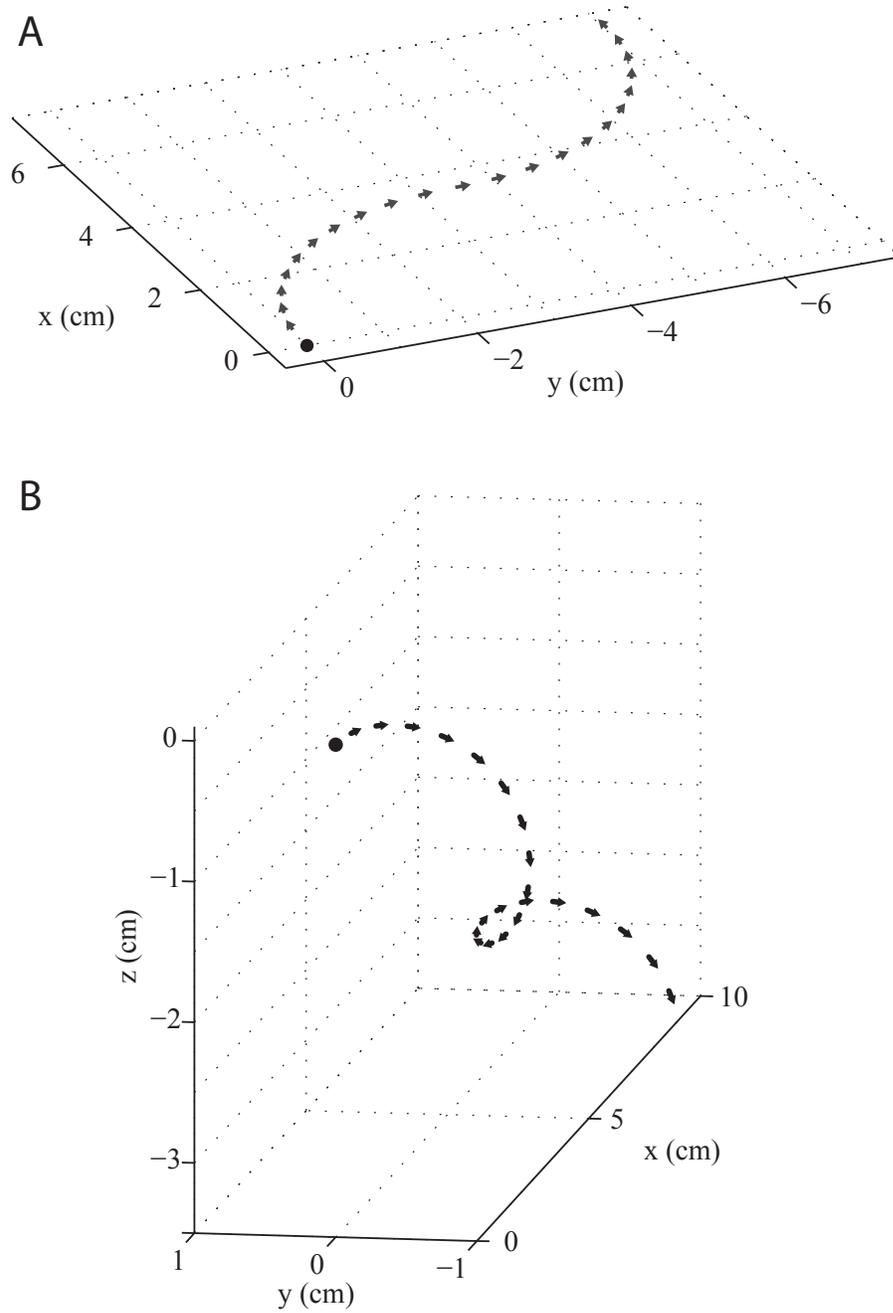
Figure 4.2: Trajectories of a steerable needle: (**A**) one flip in bevel direction after inserting 1.75π cm with parameters and velocities $\kappa = 3.5$ cm/s, $\omega = 0$, $v = 1$ cm/s and (**B**) continuous needle insertion with a rotation at the base with parameters and velocities $\kappa = 3.5$ cm/s, $\omega = \pi/4$ rad/s, $v = 1$ cm/s

drive the system from the problematic set, $\mathcal{M}$, versus the magnitude of the estimator correction term which tends to drive the system back to the set $\mathcal{M}$.

In Figure 4.4, we show the convergence of the estimator for a helical needle trajectory with two different initial error estimates: $90°$ and $179°$. As before, the estimator error was initialized such that the system output and estimator output were aligned, with the estimator errors rotations about the measurement vector. As expected, when there is a control input about the measurement vector (in the case of needle steering a rotational velocity at the base of the needle), the convergence rate is slightly slower. In fact, a very fast rotation of the needle tip would cause the needle to bore straight into the tissue and observability is lost, which may render duty-cycle based approaches to needle steering problematic [17].

We also see the results of the correction term being nearly zero at an estimator error near $180°$. The result is slow initial convergence, with rapid convergence as the error estimate approaches $90°$. Practically speaking, these represent enormous errors, and for a practical needle steering system, ensuring that initial errors not exceed $30°$ would be straight forward.

4.6 Discussion

In this chapter, we defined an output injection correction term for an estimator evolving on the manifold $SO(3)$ when only a single vector measurement is available. We showed that the estimator is convergent and provided anecdotal numerical ex-

amples for our specific application of steerable needles. For steerable needles, the estimator will improve as we are able to construct methods for tip-steerable needles that decrease the radius of curvature. The current best curvature is approximately 3.5 cm and would require about 7 cm of insertion for an adequate estimate from 90° initial error. However, 90° of initial error represents an excessive initial error; a moderately skilled experimentalist or clinician could initialize the needle within ±10°.

Our approach extends to multiple measurements, and the proof is trivial in this case. We started with the assumption of a single measurement, a constraint provided by the target application of estimation for tip-steerable needles.

While the structure of the invariant estimator given in (4.4) is fairly well defined, the derivation of the output injection correction term depends on the available measurements. We aim to take a similar approach to find other state estimators based on other output maps (say perspective or orthographic projection of points on a rigid body onto an imager). In the original observability analysis given in Lemma 4.3.1, we assumed the measurement of a single point with respect to the center of rotation of the rigid body. The proof required only one derivative of the output map. This leaves the possibility that systems with less amenable output maps are still observable and an appropriate estimator correction term can be found.

This work, in conjunction with recent results on invariant estimation from Mahony and Bonnabel's groups and recent work on probability and statistics on groups by Chirikjian [10], should provide a framework for developing filters for rigid body

motions that are at least optimal in the sense of existing extended Kalman techniques,

while maintaining the property of almost global convergence.
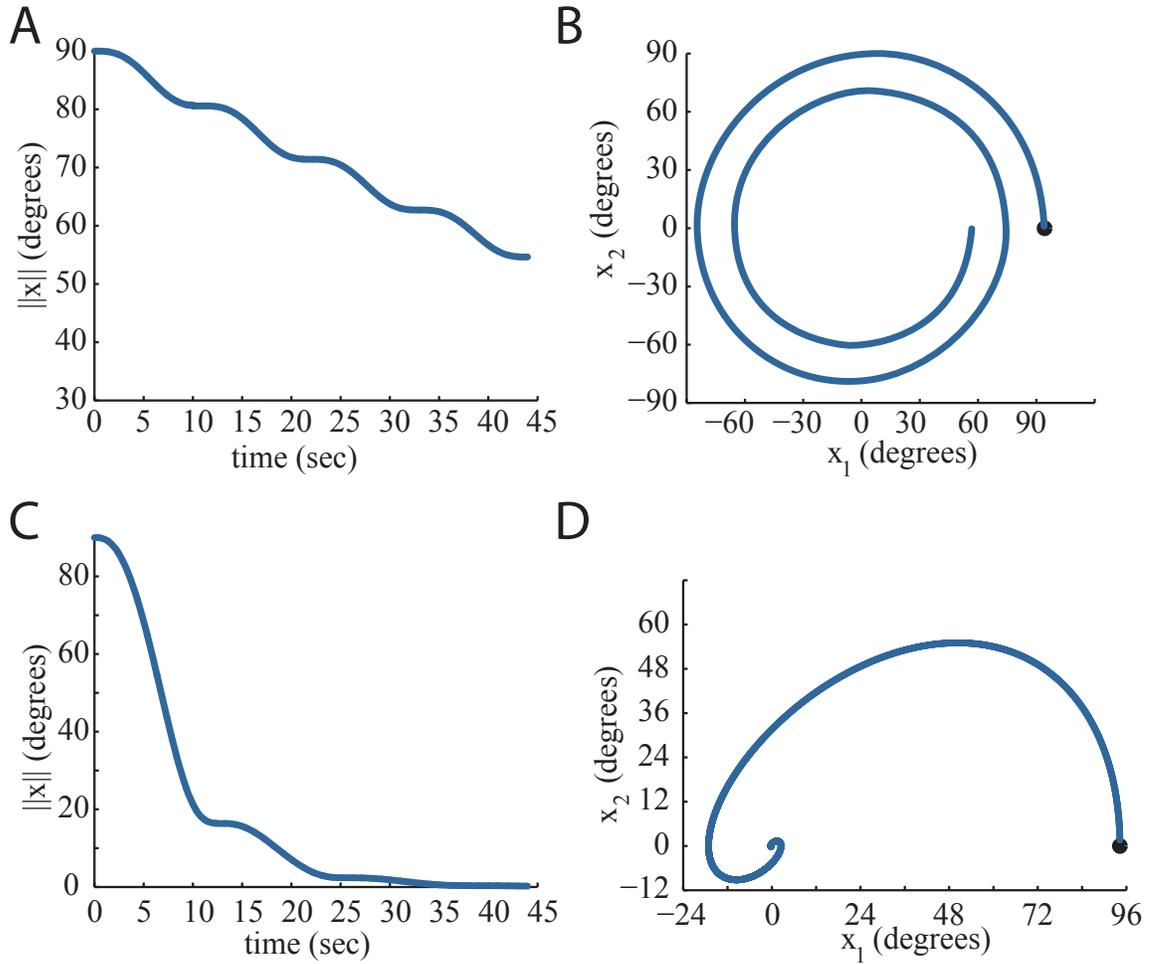
Figure 4.3: Convergence of the estimator for a piecewise planar path and different estimator gains: (**A**) convergence in angle for low estimator gain, k=0.03, (**B**) error trajectories for low estimator gain, (**C**) convergence in estimator angle for best estimator gain, k = 0.3, (**D**) error trajectory for best estimator gain.
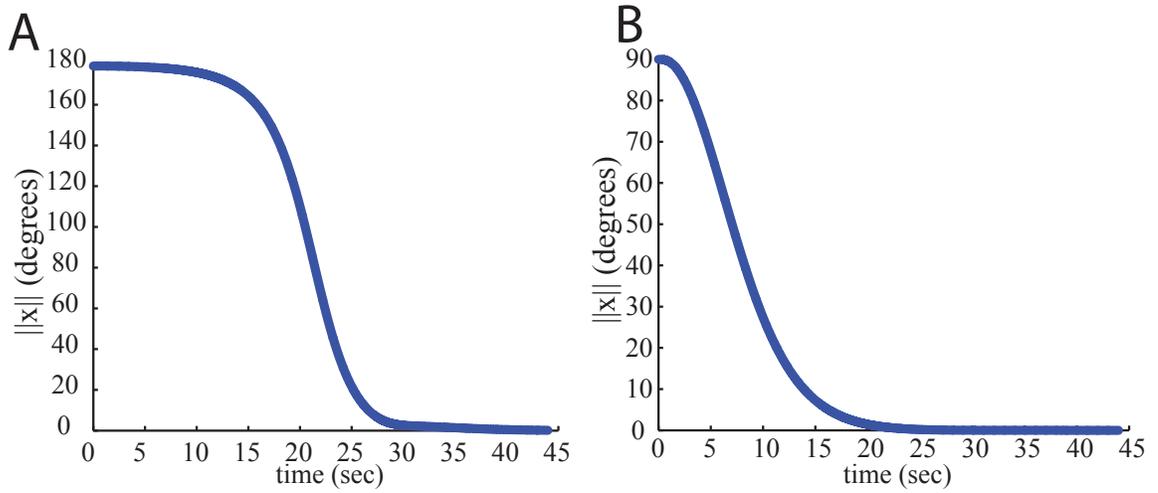
Figure 4.4: Convergence of the estimator for a helical path and a judicious estimator gain, k=0.65, and two different initial estimator errors: (A) 179 degree initial error and (B) 90 degree initial error. The kinematic parameters and velocities for both trials are $\kappa = 3.5$ cm/s, $\omega = \pi/32$ rad/s, $v = 1$ cm/s.

Chapter 5

Conclusions

We have presented two advancements to tip-steerable needles. The addition of torsional dynamics to the previous kinematics-only model of needle motion, with the associated modifications to control scheme, improves the control of the needle tip to a given plane in the tissue. The invariant observer provides a method of estimating the orientation of the needle tip given essentially any initial estimate; it only requires the needle be continuously inserted.

5.1 Torsional dynamics of tip-steerable needles

The inclusion of torsional dynamics is advantageous for needle insertion simulations and experiments. The task was to control the needle tip to a virtual plane inside the tissue. We are able to conclude the following points about the effects of considering torsional dynamics:

- Simulations indicate that all three models provide equivalent control performance for the task of controlling to the given plane, taking into consideration the robot design must allow the model type.

- Simulations indicate that model order is important, but experiments show that even one torsional state captures much of the dynamics inside the tissue for the needle and tissue parameters explored.

- Significant improvement over previously reported experimental results. We achieved convergence to a virtual plane from an initial orthogonal distance of 6 mm after only 2.5–3 cm of insertion, as compared to the previous best convergence from an initial orthogonal distance in about 8 cm.

- Faster than expected convergence in physical experiments.

For future work, we plan to conduct similar experiments under real medical imaging (cone beam C-Arm CT). These experiments will be done with both simulated tissue (plastisol) and ex-vivo tissue. The primary advantage of a real medical imaging modality is the ability to perform the experiments in tissues, simulated or real, that are thick, opaque, and don't allow the use of visible light cameras for needle tip location. We also intend to perform a non-dimensional analysis of the torsional modeling to accurately identify the free model parameters and their relative effect on the dynamics during insertion.

5.2 Invariant estimation on the Lie group of rigid body rotations

The invariant observer shows one example where coordinates are completely unnecessary to observe the orientation of a rigid body with known velocity. We find it interesting that despite this topological space being well-defined and well-understood as a manifold—where coordinates are king—this observer required none of the manifold properties of coordinate charts and the diffeomorphisms between charts to be efficacious. Its only requirement was identification of the topological space and its tangent space and ensuring the nonlinear output injection correction terms was in the tangent space.

The objective of future work is to combine this estimator with the measured tip position and a controller (perhaps the controller given in the section on torsional dynamics) to provide an almost global proof of stability for the combined estimator and controlled system. Because the estimator is known to converge given the persistency of excitation requirements are met (which is implicit in the vector field for steerable needles with constant insertion), the proof then only remains to show that the controller is convergent given the estimate. Traditionally, domain of attraction for a nonlinear system that uses a Kalman filter operating on a linearization of the system is very hard to determine analytically. Thus a formal claim of convergence can only be declared for a region of the state space local to the point of linearization

and the extent of the region is often not well defined. When linearizing about the current estimate, the likelihood of a stable estimator/controller pair is diminished even more. We hope that a combined proof of convergence for the combined estimator and estimate feedback controlled system will also be an almost global result.

Another primary task to move this theory forward is to identify appropriate correction terms for other topological spaces. Of particular immediate interest are the others most commonly used in robotics: SE(2) and SE(3). In the proof given herein, the correction structure for SO(3) only prescribed one gain parameter. There may exist alternative gain structures that will work as well or better than what we have described. An interesting exercise would be to identify a correction term that reduces to the classic Luenberger observer when linearized about the origin.

Appendix A

Mathematical definitions and computations

A.1   Lie Groups and Lie Algebras

Definition 2 (Group). *A group is a set, G, with an associated binary operator on the set, $\circ$, denoted as $(G, \circ)$ which satisfies the following conditions:*

- (Closure) *For all $a, b \in G$ then $a \circ b \in G$,*

- (Associativity) *For all $a, b, c \in G$ then $(a \circ b) \circ c = a \circ (b \circ c)$,*

- (Identity element) *There exists an element $e \in G$ such that for every $a \in G$ then $e \circ a = a$,*

- (Inverse element) *For every $a \in G$ there exists $b \in G$ such that $a \circ b = e$.*

APPENDIX A. MATHEMATICAL DEFINITIONS AND COMPUTATIONS

Definition 3 (Linear vector space on the scalar field S). *A linear vector space over the field S is a set V with two binary operations, $+$ and $\cdot$, satisfying the following conditions:*

1. (Closure)

    (Vector addition) $+ : V \times V \to V$

    (Scalar multiplication) $\cdot : V \times S \to V$

2. (Vector addition properties) *For all $x, y, z \in V$,*

    (Commutativity) $x + y = y + x$

    (Associativity) $(x + y) + z = x + (y + z)$

    (Additive identity) *There exists $0 \in V$ such that $\forall x \in V, \quad 0 + x = x$*

    (Additive inverse) *For each $x \in V$ there exists $(-x) \in V$ such that $x + (-x) = 0$*

3. (Scalar multiplication properties) *For all $x, y \in V$ and $\alpha, \beta \in S$,*

    (Associativity) $\alpha(\beta x) = (\alpha\beta)x,$

    (Multiplicative identity) *For $1 \in S$ and for all $x \in V$ then $1x = x,$*

    (Scalar multiplication distributes over vector addition) $\alpha(x + y) = \alpha x + \alpha y,$

    (Scalar addition distributes over scalar multiplication) $(\alpha + \beta)x = \alpha x + \beta x.$

Definition 4 (Lie algebra). *A Lie algebra is a linear vector space couple with a closed binary operator called the Lie bracket.*

106

APPENDIX A. MATHEMATICAL DEFINITIONS AND COMPUTATIONS

Definition 5 (Lie bracket). *The Lie bracket is a closed binary operator $[\,\cdot\,,\,\cdot\,]$ on elements of the Lie algebra. Given an algebra $\mathfrak{g}$ and $u, v, w \in \mathfrak{g}$ elements of the Lie group, the bracket satisfies the following properties:*

1. *(Closure) $[\,\cdot\,,\,\cdot\,] \in \mathfrak{g}$*

2. *(Distributive over algebra addition) $[u, v + w] = [u, v] + [u, w]$*

3. *(Continuity) $[u, v]$ is a continuous function of u and v*

4. *(Anti-symmetry) The bracket operator is anti-symmetric such that*

   $$[u, v] = -[v, u]$$

5. *(Jacobi identity) The bracket operator satisfies the Jacobi identity such that*

   $$[u, [v, w]] + [v, [w, u]] + [w, [u, v]] = 0$$

Definition 6 (Lie group). *A Lie group satisfies all the properties of a group and has the additional property that each element of the group is generated by an element of an associated Lie algebra. That is, given a Lie group G with an associated Lie algebra $\mathfrak{g}$, then for each $g \in G$ there exists an element of the Lie algebra $\hat{\xi} \in \mathfrak{g}$ such that $g = f(\hat{\xi})$. For matrix Lie groups, the generator function $f(\,\cdot\,)$ is the matrix exponential.*

APPENDIX A. MATHEMATICAL DEFINITIONS AND COMPUTATIONS

A.2 Jacobian Computation for $SO(3)$

To compute the Jacobian between body-fixed frame velocities and X-Y-Z Euler angle velocities, we first must write an element of $SO(3)$ in terms of the X-Y-Z Euler angle coordinates. Given $R(t) \in SO(3)$ and X-Y-Z Euler angle coordinates $\gamma(t)$, $\beta(t)$, and $alpha(t)$, then $R(t)$ can be written as

$$R(t) = R_x(\gamma(t))R_y(\beta(t))R_z(\alpha(t))$$

$$= \exp(\gamma(t)\hat{e}_1)\exp(\beta(t)\hat{e}_2)\exp(\alpha(t)\hat{e}_3).$$

(A.1)

We then compute $R^T(t)\dot{R}(t) = \hat{\Omega}$ and find the linear relationship between Ω and $\begin{bmatrix} \dot{\gamma}(t) & \dot{\beta}(t) & \dot{\alpha}(t) \end{bmatrix}^T$. First, we compute

$$\dot{R}(t) = \frac{d}{dt}\{R_x(\gamma(t))\}R_y(\beta(t))R_z(\alpha(t)) + R_x(\gamma(t))\frac{d}{dt}\{R_y(\beta(t))R_z(\alpha(t))\} +$$

$$R_x(\gamma(t))R_y(\beta(t))\frac{d}{dt}\{R_z(\alpha(t))\}$$

$$= \dot{\gamma}\hat{e}_1 R_x(\gamma(t))R_y(\beta(t))R_z(\alpha(t)) + R_x(\gamma(t))\dot{\beta}(t)\hat{e}_2 R_y(\beta(t))R_z(\alpha(t)) +$$

$$R_x(\gamma(t))R_y(\beta(t))\dot{\alpha}(t)\hat{e}_3 R_z(\alpha(t))$$

(A.2)

APPENDIX A. MATHEMATICAL DEFINITIONS AND COMPUTATIONS

Then,

$$\hat{\Omega} = R^T(t)\dot{R}(t) = R_z^T(\alpha(t))R_y^T(\beta(t))R_x^T(\gamma(t))\left[\dot{\gamma}(t)\hat{e}_1\right]R_x(\gamma(t))R_y(\beta(t))R_z(\alpha(t))+$$

$$R_z^T(\alpha(t))R_y^T(\beta(t))\left[\dot{\beta}(t)\hat{e}_2\right]R_y(\beta(t))R_z(\alpha(t))+$$

$$R_z^T(\alpha(t))\left[\dot{\alpha}(t)\hat{e}_3\right]R_z(\alpha(t))$$

(A.3)

and relating the body frame velocity $\hat{\Omega} \in \mathfrak{so}(3)$ to its vector form $\Omega \in \mathbb{R}^3$ via the standard isomorphism (taking into consideration the adjoint property of SO(3) and $\mathfrak{so}(3)$),

$$\Omega = \left(R_z^T(\alpha(t))R_y^T(\beta(t))R_x^T(\gamma(t))e_1\right)\dot{\gamma}(t) + \left(R_z^T(\alpha(t))R_y^T(\beta(t))e_2\right)\dot{\beta}(t)+$$

$$\left(R_z^T(\alpha(t))e_3\right)\dot{\alpha}(t)$$

$$= \left[R_z^T(\alpha(t))R_y^T(\beta(t))R_x^T(\gamma(t))e_1 \quad R_z^T(\alpha(t))R_y^T(\beta(t))e_2 \quad R_z^T(\alpha(t))e_3\right]\begin{bmatrix}\dot{\gamma}(t)\\\dot{\beta}(t)\\\dot{\alpha}(t)\end{bmatrix}.$$

(A.4)

We now see that the body-fixed frame velocities can be written as a linear function of the coordinate velocities. This matrix truly represents a Jacobian as the original

formulation could have been just as easily written as

$$\Omega = \frac{d}{dt} \left\{ f(\gamma, \beta, \alpha) \right\} = \frac{\partial f(\gamma, \beta, \alpha)}{\partial \left\{ \gamma, \beta, \alpha \right\}} \begin{bmatrix} \dot{\gamma}(t) \\ \dot{\beta}(t) \\ \dot{\alpha}(t) \end{bmatrix}, \tag{A.5}$$

had we known the appropriate form of $f(\gamma, \beta, \alpha)$. This formulation is simple, repeatable technique for deriving the Jacobian given you can write each group element as a function of the coordinates in a manner similar to that shown in (A.1).

A.3 Computations for Proper Orthogonal Decomposition and Galerkin Projection of Needle Torsional Dynamics

The computations given here are valid for the time-varying portion of the needle inside the tissue in Model A and Model C. For Model B, the modes are defined over the entire length of the needle and thus the assumed solution *is* separable is space and time. I will only present the computations for Model A and Model C here, which have the same Galerkin projection also. For Model B, the partials will be different (and more simple) and the Galerkin projection will be over the entire length of the needle. The computations are not shown here, but the Mathematica code found in the

APPENDIX A. MATHEMATICAL DEFINITIONS AND COMPUTATIONS

Appendix B does the full computation for each of the models. These computations are meant to be illustrative to aid in understanding the intermediate steps associated with the Fourier decomposition and subsequent Galerkin projection.

As described in Section 3, given the assumed modal solution with the neglected sinusoidal terms already removed,

$$\theta(x,t) = \frac{1}{2}\psi_0(x,t)q_0(t) + \sum_{k=1}^{\infty}\psi_k(x,t)q_k(t) \tag{A.6}$$

where

$$\psi_k(x,t) = \cos(\omega_k(t)x),$$
$$\omega_k(t) = \frac{k\pi}{l(t)}, \tag{A.7}$$

we substitute into the PDE describing torsional dynamics,

$$\eta \underbrace{\frac{\partial^2\theta}{\partial t^2}}_{\text{\textcircled{B}}} + \beta \underbrace{\frac{\partial\theta}{\partial t}}_{\text{\textcircled{A}}} - \kappa \underbrace{\frac{\partial^2\theta}{\partial x^2}}_{\text{\textcircled{C}}} = \delta(x)\tau_{\text{in}}(t). \tag{A.8}$$

First, we compute the first and second partials of $\psi_k(x,t)$ with respect to x and t

APPENDIX A. MATHEMATICAL DEFINITIONS AND COMPUTATIONS

for use in later steps,

$$\frac{\partial \psi(x,t)}{\partial t} = \frac{\dot{l}(t)}{l(t)}\omega_k(t)x\sin\left(\omega_k(t)x\right)$$

$$\frac{\partial^2 \psi(x,t)}{\partial t^2} = -\left(\frac{\dot{l}(t)}{l(t)}\omega_k(t)x\right)^2\cos\left(\omega_k(t)x\right) +$$

$$\frac{1}{l(t)^3}\left(-2\dot{l}(t)^2 + l(t)\ddot{l}(t)\right)\sin\left(\omega_k(t)x\right) \tag{A.9}$$

$$\frac{\partial \psi(x,t)}{\partial x} = -\omega_k(t)\sin\left(\omega_k(t)x\right)$$

$$\frac{\partial^2 \psi(x,t)}{\partial x^2} = -\omega_k(t)^2\cos\left(\omega_k(t)x\right)$$

$$\textcircled{A} \Rightarrow \frac{\partial \theta}{\partial t} = \frac{\partial}{\partial t}\left(\frac{1}{2}\psi_0(x,t)q_0(t) + \sum_{k=1}^{\infty}\psi_k(x,t)q_k(t)\right)$$

$$= \frac{1}{2}\left(\frac{\partial \psi_0(x,t)}{\partial t}q_0(t) + \psi_0(x,t)\dot{q}_0(t)\right) +$$

$$\sum_{k=1}^{\infty}\frac{\partial \psi_k(x,t)}{\partial t}q_k(t)+$$

$$\sum_{k=1}^{\infty}\psi_k(x,t)\dot{q}_k(t) \tag{A.10}$$

$$= \frac{1}{2}\dot{q}_0(t)+ \sum_{k=1}^{\infty}\cos(\omega_k(t)x)\dot{q}_k(t)+$$

$$\sum_{k=1}^{\infty}\frac{\dot{l}(t)}{l(t)}\omega_k(t)x\sin(\omega_k(t)x)q_k(t)$$

$$\textcircled{B} \Rightarrow \frac{\partial^2 \theta}{\partial t^2} = \frac{1}{2}\ddot{q}(t) + \sum_{k=1}^{\infty}\cos\left(\omega_k(t)x\right)\ddot{q}_k(t)+$$

$$\sum_{k=1}^{\infty}2\frac{\dot{l}(t)}{l(t)}\omega_k(t)\sin\left(\omega_k(t)x\right)\dot{q}_k(t)+ \tag{A.11}$$

$$\sum_{k=1}^{\infty}\frac{\partial^2 \psi_k(x,t)}{\partial t^2}q_k(t)$$

112

APPENDIX A. MATHEMATICAL DEFINITIONS AND COMPUTATIONS

Note that in Equation (A.10) we did not substitute in the results of $\frac{\partial^2 \psi_k(x,t)}{\partial t^2}$ as it would have made the result less readable.

$$
\text{\textcircled{C}} \Rightarrow \frac{\partial^2 \theta}{\partial x^2} = \frac{\partial^2}{\partial x^2} \left(\frac{1}{2} \psi_0(x,t) q_0(t) \sum_{k=1}^{\infty} \psi_k(x,t) q_k(t) \right)
$$
$$
= \frac{1}{2} \frac{\partial^2 \psi_0(x,t)}{\partial x^2} q_0(t) + \sum_{k=1}^{\infty} \frac{\partial^2 \psi_k(x,t)}{\partial x^2} q_k(t) \tag{A.12}
$$

The Galerkin projection will consist of integrals with each term in Equation (A.9),

$$
\frac{1}{l(t)} \int_{-l(t)}^{l(t)} \psi_k(x,t) * \left(\eta \frac{\partial^2 \theta}{\partial t^2} \right) dx
$$
$$
\frac{1}{l(t)} \int_{-l(t)}^{l(t)} \psi_k(x,t) * \left(\beta \frac{\partial \theta}{\partial t} \right) dx
$$
$$
\frac{1}{l(t)} \int_{-l(t)}^{l(t)} \psi_k(x,t) * \left(-\kappa \frac{\partial^2 \theta}{\partial x^2} \right) dx \tag{A.13}
$$
$$
\frac{1}{l(t)} \int_{-l(t)}^{l(t)} \psi_k(x,t) * \left(\delta(x) \tau_{\text{in}}(t) \right) dx.
$$

Appendix B contains Mathematica code for computing the Fourier modal decomposition and Galerkin projection for the three different representations of torsional dynamics.

Appendix B

Mathematica Code Listings

The software package Mathematica was used extensively to verify and perform various computations.

B.1 Torsional Dynamics of Tip-steerable Needles

The Mathematica code listings given below can be used by the reviewer for verification and incorporation into future research in steerable needles. These code listing are such that they can be copied and pasted into a Mathematica notebook and be executed as-is. Some of the unintuitive notation, such as "\[Eta]", is the plain text Mathematica format that will be converted to the appropriate Greek symbol in the Mathematica notebook.

Torsional dynamics derivation for Model A — torque control and velocity control

```
(* Setup up the parameters for the model order, mode shapes, etc. *)

\[Eta] = \[Rho]*J;
\[Kappa] = J*G;
ModeCount = 3; NM = ModeCount - 1;
CM = Range[1, NM];

qvec = Table[Subscript[q, k][t], {k, 0, NM}];
\[Psi][k_, x_, t_] := Cos[ k*\[Pi]*x /l[t]];
CC[x_, t_] := Join[{1/2 \[Psi][0, x, t] }, \[Psi][#, x, t] & /@ CM];
\[Theta][x_, t_] := CC[x, t].qvec;
MODELIST = Join[{\[Psi][0, x, t]} , \[Psi][#, x, t] & /@ CM];


(* Perform the change of coordinates and Gelerking projection. *)

T3 = Integrate[#*(- \[Kappa]*D[\[Theta][x, t], {x, 2}]), {x, -l[t], l[t]}] & /@
    MODELIST;
T2 = Assuming[l[t] > 0 && L > l[t],
   Integrate[#*( \[Beta] D[\[Theta][x, t], {t, 1}]), {x, -l[t], l[t]}] & /@
    MODELIST];
T1 = Integrate[#*( \[Eta] * D[\[Theta][x, t], {t, 2}]), {x, -l[t], l[t]}] & /@
    MODELIST;

CTRL = Assuming[
   L \[Element] Reals && l[t] \[Element] Reals && l[t] > 0 && L > 0 &&
    L > l[t],
   (1/l[t])*Integrate[#*(DiracDelta[x] u[t]) , {x, -l[t], l[t]}] & /@
    MODELIST];

K3 = Coefficient[#, qvec] & /@ T3;
D3 = Coefficient[#, D[qvec, t]] & /@ T3;
M3 = Coefficient[#, D[qvec, {t, 2}]] & /@ T3;

K2 = Coefficient[#, qvec] & /@ T2;
D2 = Coefficient[#, D[qvec, t]] & /@ T2;
M2 = Coefficient[#, D[qvec, {t, 2}]] & /@ T2;

K1 = Coefficient[#, qvec] & /@ T1 ;
D1 = Coefficient[#, D[qvec, t]] & /@ T1;
M1 = Coefficient[#, D[qvec, {t, 2}]] & /@ T1;

Subscript[M,
  1] = (1/l[t]) FullSimplify[(M1 + M2 + M3) /. {\[Rho] -> p,
      Derivative[1][l][t] -> v, (l^\[Prime]\[Prime])[t] -> 0}];
Subscript[D,
```

```
  1] = (1/l[t]) FullSimplify[(D1 + D2 + D3) /. {\[Rho] -> p,
      Derivative[1][l][t] -> v, (l^\[Prime]\[Prime])[t] -> 0}];
Subscript[K,
  1] = (1/l[t]) FullSimplify[(K1 + K3 + K3) /. {\[Rho] -> p,
      Derivative[1][l][t] -> v, (l^\[Prime]\[Prime])[t] -> 0}];
P = Coefficient[CTRL, u[t]];


(* Compute the system matrices for torque control and velocity control. *)

(* Compute the system and output matrices for Model A with torque control *)

ClearAttributes[C, Protected];
ClearAttributes[D, Protected];

Subscript[C, \[ScriptL]] = Flatten[Join[{1/2} , (-1)^# & /@ Range[1, NM]]];

A[t_] := -Inverse[Subscript[D, 1]].Subscript[K, 1];
B[t_] := -Inverse[Subscript[D, 1]].P;
C[t_] := Subscript[C, \[ScriptL]].A[t];
D[t_] := Subscript[C, \[ScriptL]].B[t];

(* Compute the system and output matrices for Model A with velocity control *)

ClearAttributes[C, Protected];
ClearAttributes[D, Protected];

Subscript[C, 0] = Flatten[Join[{1/2} , # & /@ Table[1, {k, 1, NM}]]];
Subscript[C, \[ScriptL]] = Flatten[-1 + (-1)^# & /@ Range[1, NM]];
A[t_] := 1/
    Subscript[C,
     0].Inverse[Subscript[D, 1]].P Inverse[Subscript[D, 1]].Outer[Times, P,
      Subscript[C, 0]].Inverse[Subscript[D, 1]].Subscript[K, 1] -
   Inverse[Subscript[D, 1]].Subscript[K, 1];
B[t_] := 1/
   Subscript[C, 0].Inverse[Subscript[D, 1]].P Inverse[Subscript[D, 1]].P;
C[t_] := Subscript[C, \[ScriptL]].A[t];
D[t_] := (1 + Subscript[C, \[ScriptL]].B[t]);
```

Torsional dynamics derivation for Model B — torque control and velocity control

```
(* Setup up the parameters for the model order, mode shapes, etc. *)
\[Eta] = \[Rho]*J;
\[Kappa] = J*G;
ModeCount = 3; NM = ModeCount - 1;
CM = Range[1, NM];

qvec = Table[Subscript[q, k][t], {k, 0, NM}];
```

```
\[Psi][k_, x_, t_] := Cos[ k*\[Pi]*x /L];
CC[x_, t_] := Join[{1/2 \[Psi][0, x, t] }, \[Psi][#, x, t] & /@ CM];
\[Theta][x_, t_] := CC[x, t].qvec;
MODELIST = Join[{\[Psi][0, x, t]} , \[Psi][#, x, t] & /@ CM];


(* Perform the change of coordinates and Gelerking projection. *)

T3 = Integrate[#*(- \[Kappa]*D[\[Theta][x, t], {x, 2}]), {x, -L, L}] & /@
    MODELIST;

T21 = Assuming[l[t] > 0 && L > l[t],
    Integrate[#*( \[Beta] D[\[Theta][x, t], {t, 1}]) , {x, (L - l[t]), L}] & /@
       MODELIST];
T22 = Assuming[l[t] > 0 && L > l[t],
    Integrate[#*( \[Beta] D[\[Theta][x, t], {t, 1}]) , {x, -L, -(L -
          l[t])}] & /@ MODELIST];
T23 = Assuming[l[t] > 0 && L > l[t],
    Integrate[#*(  \[Nu] D[\[Theta][x, t], {t, 1}]) , {x, -(L - l[t]),
        L - l[t]}] & /@ MODELIST];
T2 = T21 + T22 + T23;

T1 = Integrate[#*( \[Eta] * D[\[Theta][x, t], {t, 2}]), {x, -L, L}] & /@
    MODELIST;

CTRL = Assuming[
    L \[Element] Reals && l[t] \[Element] Reals && l[t] > 0 && L > 0 &&
     L > l[t],
    (1/L)*Integrate[#*(DiracDelta[x] u[t]) , {x, -L, L}] & /@ MODELIST];

K3 = Coefficient[#, qvec] & /@ T3;
D3 = Coefficient[#, D[qvec, t]] & /@ T3;
M3 = Coefficient[#, D[qvec, {t, 2}]] & /@ T3;

K2 = Coefficient[#, qvec] & /@ T2;
D2 = Coefficient[#, D[qvec, t]] & /@ T2;
M2 = Coefficient[#, D[qvec, {t, 2}]] & /@ T2;

K1 = Coefficient[#, qvec] & /@ T1 ;
D1 = Coefficient[#, D[qvec, t]] & /@ T1;
M1 = Coefficient[#, D[qvec, {t, 2}]] & /@ T1;

Subscript[M,
  1] = (1/L) FullSimplify[(M1 + M2 + M3) /. {\[Rho] -> p,
      Derivative[1][l][t] -> v, (l^\[Prime]\[Prime])[t] -> 0}];
Subscript[D,
  1] = (1/L) FullSimplify[(D1 + D2 + D3) /. {\[Rho] -> p,
      Derivative[1][l][t] -> v, (l^\[Prime]\[Prime])[t] -> 0}];
Subscript[K,
  1] = (1/L) FullSimplify[(K1 + K3 + K3) /. {\[Rho] -> p,
```

```
        Derivative[1][l][t] -> v, (l^\[Prime]\[Prime])[t] -> 0}];
P = Coefficient[CTRL, u[t]];


(* Compute the system matrices for torque control and velocity control. *)

(* Compute the system and output matrices for Model A with torque control *)

ClearAttributes[C, Protected];
ClearAttributes[D, Protected];

Subscript[C, \[ScriptL]] = Flatten[Join[{1/2} , (-1)^# & /@ Range[1, NM]]];

A[t_] := -Inverse[Subscript[D, 1]].Subscript[K, 1];
B[t_] := -Inverse[Subscript[D, 1]].P;
C[t_] := Subscript[C, \[ScriptL]].A[t];
D[t_] := Subscript[C, \[ScriptL]].B[t];

(* Compute the system and output matrices for Model A with velocity control *)

ClearAttributes[C, Protected];
ClearAttributes[D, Protected];

Subscript[C, 0] = Flatten[Join[{1/2} , # & /@ Table[1, {k, 1, NM}]]];
Subscript[C, \[ScriptL]] = Flatten[-1 + (-1)^# & /@ Range[1, NM]];
A[t_] := 1/
    Subscript[C,
     0].Inverse[Subscript[D, 1]].P Inverse[Subscript[D, 1]].Outer[Times, P,
       Subscript[C, 0]].Inverse[Subscript[D, 1]].Subscript[K, 1] -
   Inverse[Subscript[D, 1]].Subscript[K, 1];
B[t_] := 1/
   Subscript[C, 0].Inverse[Subscript[D, 1]].P Inverse[Subscript[D, 1]].P;
C[t_] := Subscript[C, \[ScriptL]].A[t];
D[t_] := (1 + Subscript[C, \[ScriptL]].B[t]);
```

Torsional dynamics derivation for Model C — position control

```
(* Setup up the parameters for the model order, mode shapes, etc. *)

\[Eta] = \[Rho]*J;
\[Kappa] = J*G;
ModeCount = 1; NM = ModeCount - 1;
CM = Range[1, NM];

qvec = Table[Subscript[q, k][t], {k, 0, NM}];
\[Psi][k_, x_, t_] := Cos[ k*\[Pi]*x /l[t]];
CC[x_, t_] := Join[{1/2 \[Psi][0, x, t] }, \[Psi][#, x, t] & /@ CM];
\[Theta][x_, t_] := CC[x, t].qvec;
MODELIST = Join[{\[Psi][0, x, t]} , \[Psi][#, x, t] & /@ CM];
```

```
(* Perform the change of coordinates and Gelerkin projection. *)

T3 = Integrate[#*(- \[Kappa]*D[\[Theta][x, t], {x, 2}]), {x, -l[t], l[t]}] & /@
    MODELIST;
T2 = Assuming[l[t] > 0 && L > l[t],
   Integrate[#*( \[Beta] D[\[Theta][x, t], {t, 1}]), {x, -l[t], l[t]}] & /@
    MODELIST];
T1 = Integrate[#*( \[Eta] * D[\[Theta][x, t], {t, 2}]), {x, -l[t], l[t]}] & /@
    MODELIST;

CTRL = Assuming[
   L \[Element] Reals && l[t] \[Element] Reals && l[t] > 0 && L > 0 &&
    L > l[t],
   (1/l[t])*Integrate[#*(DiracDelta[x] u[t]) , {x, -l[t], l[t]}] & /@
    MODELIST];

K3 = Coefficient[#, qvec] & /@ T3;
D3 = Coefficient[#, D[qvec, t]] & /@ T3;
M3 = Coefficient[#, D[qvec, {t, 2}]] & /@ T3;

K2 = Coefficient[#, qvec] & /@ T2;
D2 = Coefficient[#, D[qvec, t]] & /@ T2;
M2 = Coefficient[#, D[qvec, {t, 2}]] & /@ T2;

K1 = Coefficient[#, qvec] & /@ T1 ;
D1 = Coefficient[#, D[qvec, t]] & /@ T1;
M1 = Coefficient[#, D[qvec, {t, 2}]] & /@ T1;

Subscript[M,
  1] = (1/l[t]) FullSimplify[(M1 + M2 + M3) /. {\[Rho] -> p,
      Derivative[1][l][t] -> v, (l^\[Prime]\[Prime])[t] -> 0}];
Subscript[D,
  1] = (1/l[t]) FullSimplify[(D1 + D2 + D3) /. {\[Rho] -> p,
      Derivative[1][l][t] -> v, (l^\[Prime]\[Prime])[t] -> 0}];
Subscript[K,
  1] = (1/l[t]) FullSimplify[(K1 + K3 + K3) /. {\[Rho] -> p,
      Derivative[1][l][t] -> v, (l^\[Prime]\[Prime])[t] -> 0}];
P = Coefficient[CTRL, u[t]];

(* Compute the system matrices for position control at the base. *)

(* Compute the system and output matrices for Model A with position control \
at the base *)
ClearAttributes[C, Protected];
ClearAttributes[D, Protected];

Subscript[C, 0] = Flatten[Join[{1/2} , # & /@ Table[1, {k, 1, NM}]]];
Subscript[C, \[ScriptL]] = Flatten[Join[{1/2} , (-1)^# & /@ Range[1, NM]]];
Subscript[K, s] = (J G)/(L - l[t]); (* The time varying spring constant *)
```

APPENDIX B. MATHEMATICA CODE LISTINGS

```
A[t_] := -Inverse[Subscript[D,
    1]].(Subscript[K, 1] + Subscript[K, s] Outer[Times, P, Subscript[C, 0]]);
B[t_] := Subscript[K, s] Inverse[Subscript[D, 1]].P;
C[t_] := Subscript[C, \[ScriptL]].A[t];
D[t_] := Subscript[C, \[ScriptL]].B[t];
```

Bibliography

[1] R. Abraham, J. Marsden, and T. Ratiu. *Manifolds, tensor analysis, and applications*, volume 75. Springer, 1988.

[2] R. Ash. *Real analysis and probability*, volume 239. Academic Press New York, 1972.

[3] E. Barbashin and N. Krasovskyii. On the stability of motion on the large. *Doklady Akademii Nauk SSSR*, 86:235–265, 1952. (in Russian).

[4] C. Belta and V. Kumar. An SVD-based projection method for interpolation on SE(3). *IEEE Trans. Robot. Automat.*, 18(3), 2002.

[5] S. Bonnabel, P. Martin, and P. Rouchon. Symmetry-preserving observers. *IEEE Trans. Autom. Control*, 53(11):2514–2526, 2008.

[6] S. Bonnabel, P. Martin, and P. Rouchon. Non-linear symmetry-preserving observers on Lie groups. *IEEE Trans. Autom. Control*, 54(7):1709–1713, 2009.

[7] S. Bonnabel, P. Martin, and E. Salaun. Invariant extended kalman filter: theory

and application to a velocity-aided attitude estimation problem. In *Decision and Control, 2009 held jointly with the 2009 28th Chinese Control Conference. CDC/CCC 2009. Proceedings of the 48th IEEE Conference on*, pages 1297–1304. IEEE, 2009.

[8] L. Chen and X. Yang. Transverse nonlinear dynamics of axially accelerating viscoelastic beams based on 4-term galerkin truncation. *Chaos, Solitons & Fractals*, 27(3):748–757, 2006.

[9] G. Chirikjian and A. Kyatkin. *Engineering Applications of Noncommutative Harmonic Analysis*. CRC Press, Boca Raton, FL, 2001.

[10] G. S. Chirikjian. *Stochastic Models, Information Theory, and Lie Groups, Volume I: Classical Results and Geometric Methods*. Birkhauser, 2009.

[11] H. Choset. *Principles of robot motion: theory, algorithms, and implementation*. The MIT Press, 2005.

[12] N. J. Cowan, K. Goldberg, G. S. Chirikjian, G. Fichtinger, R. Alterovitz, K. B. Reed, V. Kallem, W. Park, S. Misra, and A. M. Okamura. Robotic needle steering: Design, modeling, planning, and image guidance. In J. Rosen, B. Hannaford, and R. Satava, editors, *Surgical Robotics – Systems, Applications, and Visions*, pages 557–582. Springer, 2011.

BIBLIOGRAPHY

[13] J. Crassidis, F. Markley, and Y. Cheng. Survey of nonlinear attitude estimation methods. *Journal of Guidance Control and Dynamics*, 30(1):12, 2007.

[14] J. L. Crassidis and F. L. Markley. Unscented filtering for spacecraft attitude estimation. *Journal of Guidance Control and Dynamics*, 26(4):536–542, 2003.

[15] F. E. Daum. Nonlinear filters: beyond the Kalman filter. *IEEE Aerospace and Electronic Systems Magazine*, 20(8 Part 2):57–69, 2005.

[16] S. DiMaio and S. Salcudean. Needle insertion modeling and simulation. *IEEE Trans. Robot. Automat.*, 19:864–875, 2003.

[17] J. Engh, D. Minhas, D. Kondziolka, and C. Riviere. Percutaneous intracerebral navigation by duty-cycled spinning of flexible bevel-tipped needles. *Neurosurgery*, 67(4):1117, 2010.

[18] M. Epstein. *The geometrical language of continuum mechanics.* Cambridge University Press, 2010.

[19] D. Glozman and M. Shoham. Image-guided robotic flexible needle steering. *IEEE Trans. Robot.*, 23(3):459–467, 2007.

[20] E. Griffith and K. Kumar. On the observability of nonlinear systems: I. *Journal of Mathematical Analysis and Applications*, 35(1):135–147, 1971.

[21] M. Hamermesh. *Group theory and its application to physical problems.* Dover Pubns, 1989.

BIBLIOGRAPHY

[22] P. Holmes, J. Lumley, and G. Berkooz. *Turbulence, coherent structures, dynamical systems and symmetry.* Cambridge Univ Pr, 1998.

[23] V. Kallem, D. E. Chang, and N. J. Cowan. Task-induced symmetry and reduction with application to needle steering. *IEEE Trans. Autom. Control,* 55(3):664 –673, Mar. 2010. NIHMS192980.

[24] V. Kallem, D. E. Chang, and N. J. Cowan. Observer design for needle steering using task-induced symmetry and reduction. In *World Cong. Intl. Fed. Autom. Control,* Milan, Italy, Aug. 2011.

[25] V. Kallem and N. J. Cowan. Image guidance of flexible tip-steerable needles. *IEEE Trans. Robot.,* 25:191–196, 2009. NIHMS192987.

[26] H. K. Khalil. *Nonlinear Systems.* Prentice Hall, 2 edition, 2002.

[27] J. C. Kinsey and L. L. Whitcomb. Adaptive identification on the group of rigid-body rotations and its application to underwater vehicle navigation. *IEEE Trans. Robot.,* 23:124–136, 2007.

[28] C. Lageman, J. Trumpf, and R. Mahony. Gradient-like observers for invariant dynamics on a Lie group. *IEEE Trans. Autom. Control,* 55(2):367–377, 2010.

[29] B. Lathi. *Signal processing and linear systems.* Oxford University Press, USA, 2001.

BIBLIOGRAPHY

[30] E. Lefferts, F. L. Markley, and M. D. Shuster. Kalman filtering for spacecraft attitude estimation. *Journal of Guidance, Control, and Dynamics*, 5(5):417–429, 1982.

[31] R. Mahony, T. Hamel, and J. Pflimlin. Nonlinear complementary filters on the special orthogonal group. *IEEE Trans. Autom. Control*, 53(5):1203–1218, 2008.

[32] E. Malis, T. Hamel, R. Mahony, and P. Morin. Estimation of homography dynamics on the special linear group. *Visual Servoing via Advanced Numerical Methods*, pages 133–150, 2010.

[33] V. G. Mallapragada, N. Sarkar, and T. K. Podder. Robot-assisted real-time tumor manipulation for breast biopsy. *IEEE Trans. Robot.*, 25(2):316–324, 2009.

[34] F. L. Markley. Attitude filtering on SO (3). *The Journal of Astronautical Sciences*, 54:391–413, 2006.

[35] J. E. Marsden and T. S. Ratiu. *Introduction to Mechanics and Symmetry*. Springer, 1999.

[36] R. M. Murray, Z. Li, and S. S. Sastry. *A Mathematical Introduction to Robotic Manipulation*. CRC Press, Boca Raton, FL, 1994.

[37] S. Okazawa, R. Ebrahimi, J. Chuang, S. E. Salcudean, and R. Rohling. Hand-held steerable needle device. *IEEE/ASME Trans. Mech.*, 10(3):285–296, 2005.

BIBLIOGRAPHY

[38] F. C. Park. *The optimal kinematic design of mechanisms.* PhD thesis, Harvard University Cambridge, MA, USA, 1991.

[39] W. Park, J. S. Kim, Y. Zhou, N. J. Cowan, A. M. Okamura, and G. S. Chirikjian. Diffusion-based motion planning for a nonholonomic flexible needle model. In *Proc. IEEE Int. Conf. Robot. Autom.*, pages 4600–4605, Barcelona, Spain, Apr. 2005. IEEE.

[40] W. Park, Y. Liu, Y. Zhou, M. Moses, and G. S. Chirikjian. Kinematic state estimation and motion planning for stochastic nonholonomic systems using the exponential map. *Robotica*, 2008. Accepted.

[41] W. Park, K. B. Reed, A. M. Okamura, and G. S. Chirikjian. Estimation of model parameters for steerable needles. *Proc. IEEE Int. Conf. Robot. Autom.*, pages 3703 –3708, may. 2010.

[42] K. B. Reed, A. Majewicz, V. Kallem, R. Alterovitz, K. Goldberg, N. J. Cowan, and A. M. Okamura. Robot-assisted needle steering. *IEEE Robot. Autom. Mag.*, 2011. In press.

[43] K. B. Reed, A. M. Okamura, and N. J. Cowan. Modeling and control of needles with torsional friction. *IEEE Trans. Biomed. Eng.*, 56(12):2905–2916, Dec. 2009. NIHMS192959.

[44] N. Rouche. On the stability of motion. *International Journal of Non-Linear Mechanics*, 3(3):295–306, 1968.

[45] C. Rowley. Model reduction for fluids, using balanced proper orthogonal decomposition. *International Journal of Bifurcation Chaos in Applied Sciences and Engineering*, 15(3):997–1014, 2005.

[46] M. Spivak. *A comprehensive introduction to differential geometry*, volume 1. Publish or Perish Berkeley, 1979.

[47] K. Sze, S. Chen, and J. Huang. The incremental harmonic balance method for nonlinear vibration of axially moving beams. *Journal of Sound and Vibration*, 281(3-5):611–626, 2005.

[48] V.M and Matrosov. On the stability of motion. *Journal of Applied Mathematics and Mechanics*, 26(5):1337 – 1353, 1962.

[49] L. Wang, Z. Hu, Z. Zhong, and J. Ju. Hamiltonian dynamic analysis of an axially translating beam featuring time-variant velocity. *Acta Mechanica*, 206(3):149–161, 2009.

[50] R. J. Webster III, J. S. Kim, N. J. Cowan, G. S. Chirikjian, and A. M. Okamura. Nonholonomic modeling of needle steering. *Int. J. Robot. Res.*, 25(5/6):509–526, May 2006.

[51] T. Wedlick and A. Okamura. Characterization of pre-curved needles for steering

in tissue. In *Engineering in Medicine and Biology Society*, pages 1200 –1203, sept. 2009.

[52] A. Wood. New method of treating neuralgia by the direct application of opiates to the painful points. *Edin. Med. Surg. J.*, 82:265–281, 1855.

Vita

John Swensen received the Bachelor of Science degree in Electrical Engineering from Utah State University in 2003 and began work at Ball Aerospace and Technologies Corporation. While at Ball he worked on the James Webb Space Telescope creating software for controlling the scale model testbed telescope for the development of wavefront sensing and control algorithms. He also developed focal plane simulators for the Ball Aerospace series of star tracker products. In 2006, he returned to school to pursue a doctoral degree in the Mechanical Engineering Department at Johns Hopkins University in the Locomotion in Mechanical and Biological Systems (LIMBS) Laboratory. His research is focused on modeling, estimation, and control of tip-steerable needles.

Starting in December 2011, John will assume a postdoctoral associate position in the Grab Lab at Yale University. He will continue doing robotics research in the area of compliant robotic materials through controlled miniaturized "active cells".